minerals

Article

Tectonic Evolution of the Fawakhir Ophiolite, Central Eastern Desert of Egypt: Implications for Island Arc Amalgamation and Subduction Polarity during the Neoproterozoic

Samar Yousef [1], Chang Whan Oh [1,*], Kenta Kawaguchi [2] and Mohamed Abdelkareem [3,4]

1 Department of Earth and Environmental Sciences, Jeonbuk National University, 567, Baekje-daero, Deokjin-gu, Jeonju 54896, Republic of Korea; samaryousef@jbnu.ac.kr
2 Division of Earth Sciences, Faculty of Social and Cultural Studies, Kyushu University, 744 Motooka, Nishi-ku, Fukuoka 819-0395, Japan
3 Geology Department, South Valley University, Qena 83523, Egypt
4 Remote Sensing Lab, South Valley University, Qena 83523, Egypt
* Correspondence: ocwhan@jbnu.ac.kr; Tel.: +82-63-270-3397

Abstract: The Fawakhir area consists of an ophiolite sequence surrounded by an ophiolitic mélange. In the mélange, serpentinized ultramafic rock, gabbro, gabbroic diorite, diabase, andesite, and basalt occur as tectonic blocks within the metasediments. The gabbro gives a zircon U–Pb age of ~816 Ma, and the trace element composition of the zircon suggests its generation under a continental-arc tectonic setting. The geochemistry of gabbro and other tectonic blocks in the ophiolitic mélange indicates their formation from a backarc basin in a continental island arc tectonic setting. The ophiolite sequence consists of serpentinized ultramafic rock, gabbro, and basaltic rocks and was intruded by felsic dikes. The gabbro from the ophiolite sequence and felsic dikes give zircon U–Pb ages of 742 Ma and 723 Ma, respectively. Trace elements composition of this zircon refers to their formation in a continental-arc tectonic setting. The geochemistry of rocks in the ophiolitic sequence indicates their formation in a forearc basin. Together with previous studies, this study suggests that the tectonic blocks in the mélange formed in a backarc during the early-stage northwards subduction event, which may have started at ~816 Ma or earlier. On the other hand, the rocks in the ophiolite sequence can be considered to have formed in a forearc by the later eastwards subduction event at ~742–723 Ma.

Keywords: Fawakhir; Eastern Desert of Egypt; ophiolite sequence; mélange; U–Pb zircon age dating; island arc

Citation: Yousef, S.; Oh, C.W.; Kawaguchi, K.; Abdelkareem, M. Tectonic Evolution of the Fawakhir Ophiolite, Central Eastern Desert of Egypt: Implications for Island Arc Amalgamation and Subduction Polarity during the Neoproterozoic. *Minerals* **2023**, *13*, 1022. https://doi.org/10.3390/min13081022

Academic Editor: Federica Zaccarini

Received: 30 June 2023
Revised: 21 July 2023
Accepted: 26 July 2023
Published: 30 July 2023

1. Introduction

The Arabian Nubian Shield (ANS) is located along the boundary between East Africa and West Asia (Figures 1 and 2). It consists of two shields: the Arabian shield in the east, part of the Asian continent, and the Nubian shield in the west, part of the African continent. The ANS includes west of Saudi Arabia, east of Egypt and Sudan, Eritrea, Ethiopia, Kenya, and parts of Jordon and Yemen. Due to their multi-tectono-thermal events, the tectonic evolution of the ANS cannot be explained by a single amalgamation process [1], and more petrological studies combined with additional geochronological and geochemical investigations are crucial to revealing the comprehensive evolutional scenarios of the ANS.

The ANS is an intra-oceanic island arc complex that formed within the Mozambique paleo-ocean. It consists of three main intra-oceanic island arcs; the Northern, Central, and Southern ANS terranes. It also includes the Afif microcontinent that amalgamated to the island arc complex, enlarging the ANS. The ANS was finally amalgamated into the Western and Eastern Gondwana continents [2,3]. This can be supported by the presence of ophiolite sequences and post-collision-related rocks. The ANS in Egypt is represented by the Neoproterozoic rocks in the Eastern Desert (ED) and Sinai (Figures 2 and 3a).

There have been numerous studies conducted on the ED, proposing different scenarios for the formation of Neoproterozoic rocks. They can be grouped into three main scenarios: the first scenario suggested that the Neoproterozoic rocks formed by a single continuous subduction event; the second scenario proposed their formation due to the two subduction events with the same subduction direction; the third scenario suggested that the two subduction events with different subduction direction lead to Neoproterozoic rocks formation. For instance, one continuous E-dipping subduction event has been suggested at 660–640 Ma, and the ophiolites are considered formed as an oceanic crust in the rift tectonic setting at 800–780 Ma. However, the 800–780 Ma age range uncertainty is very high because it was obtained from U–Pb age dating on only two spots [4]. On the other hand, it has been proposed that two E-dipping subductions occurred at 830–750 Ma and 750–700 Ma. However, this model is based only on the zircon U–Pb ages of 733–698 Ma without any evidence older than 750 Ma [5,6]. In addition, it has been suggested that two N-dipping subductions occurred at 770–730 Ma and 630 Ma, according to K–Ar dating analysis on biotite and hornblende [7]. Other studies suggested two different subductions with different subduction directions. For example, early S-dipping subduction was suggested to occur at 850–700 Ma, and to be followed by N-dipping subduction at 640 Ma [8]. However, the ages obtained for different stages pose a challenge in terms of acceptance due to their determination based on the combination of ages from diverse samples collected across different areas. Meanwhile, another study suggested that early E-dipping subduction occurred at 830–700 Ma, and later W-dipping subduction occurred until the collision at ~630 Ma [9,10]. Due to the limited elaboration and insufficient evidence, including age data in the studies which suggested the above tectonic interpretation, it is hard to elucidate the tectonic evolution of ED comprehensively.

The Fawakhir area within the Central Eastern Desert (CED) (Figure 3b) is a crucial location for understanding the complete tectonic history of the ED, given its possession of a complete ophiolite sequence with post-collision-related rocks. However, the Neoproterozoic rocks in the area lack precise U–Pb age dating and geochemical data, resulting in a multitude of disputes regarding the intrusion age and tectonic settings of ophiolite rocks and the interpretation of tectonic evolution. Additionally, evidence for an arc older than 800 Ma has not been provided in any of the previous studies. As the tectonic evolution of the Fawakhir area is interconnected with that of the entire CED, a comprehensive study of the Fawakhir area is essential for resolving disputes related not only to the Fawakhir area but also to the tectonic evolution of the CED. Therefore, conducting U–Pb zircon age dating and geochemical analysis on the rocks in the Fawakhir area is necessary to determine whether they resulted from single or multiple subduction events, to conclude the subduction direction and timing of each event, to clarify the existence and tectonic setting for rocks older than 800 Ma, and to reveal the regional tectonic evolution of the CED.

In this study, we carried out whole rock geochemical investigation, mineral chemical analysis, and zircon U–Pb age dating on various types of rocks, including gabbro, gabbroic diorite, diabase, basalt, and andesite from the ophiolitic mélange, and the gabbro, serpentinized ultramafic rocks, and basaltic rocks from the ophiolite sequence, and felsic dikes in the Fawakhir area. Additionally, trace element compositions of the igneous zircons were analyzed to determine the tectonic setting. The obtained data, including ages and geochemical information, will be utilized to propose the tectonic evolution of the Fawakhir ophiolite and to provide insight into the tectonic evolution in the CED.

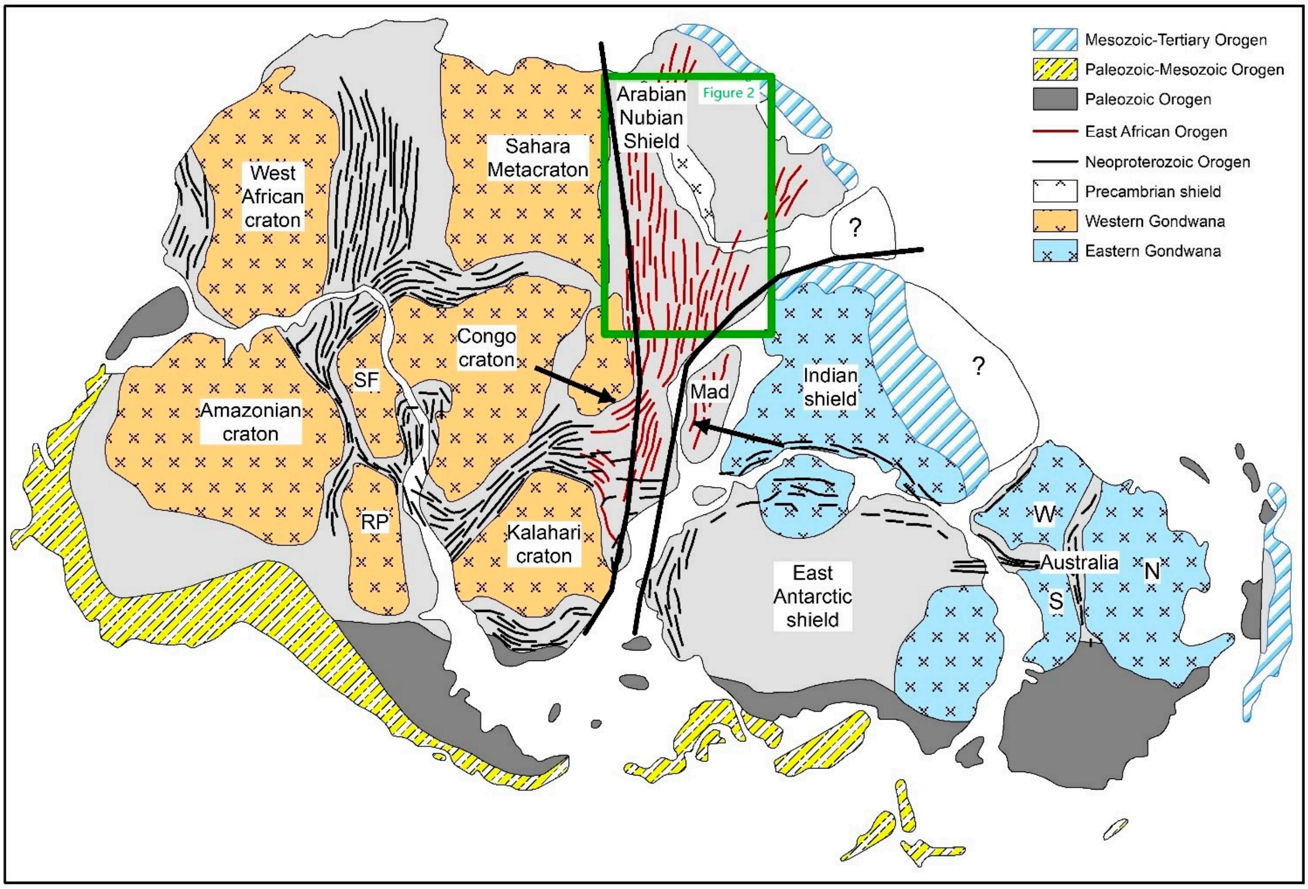

Figure 1. The paleo-position of the Arabian-Nubian Shield (ANS) between the Eastern and Western Gondwana continents during the Neoproterozoic [11]. Black arrows indicate the direction of conversion between the Eastern and Western Gondwana continents. SF, Sao Francisco Craton; RP, Rio de la Plata Craton.

Figure 2. The ANS terrane with the sutures in and around it and the ages of sutures (modified from [3]). The background map is from an ArcGIS (10.5) online basemap (source: Esri, DigitalGlobe, GeoEye, i-cubed, USDA FSA, USGS, AEX, Getmapping, Aerogrid, IGN, IGP, swisstopo, and the GIS User Community).

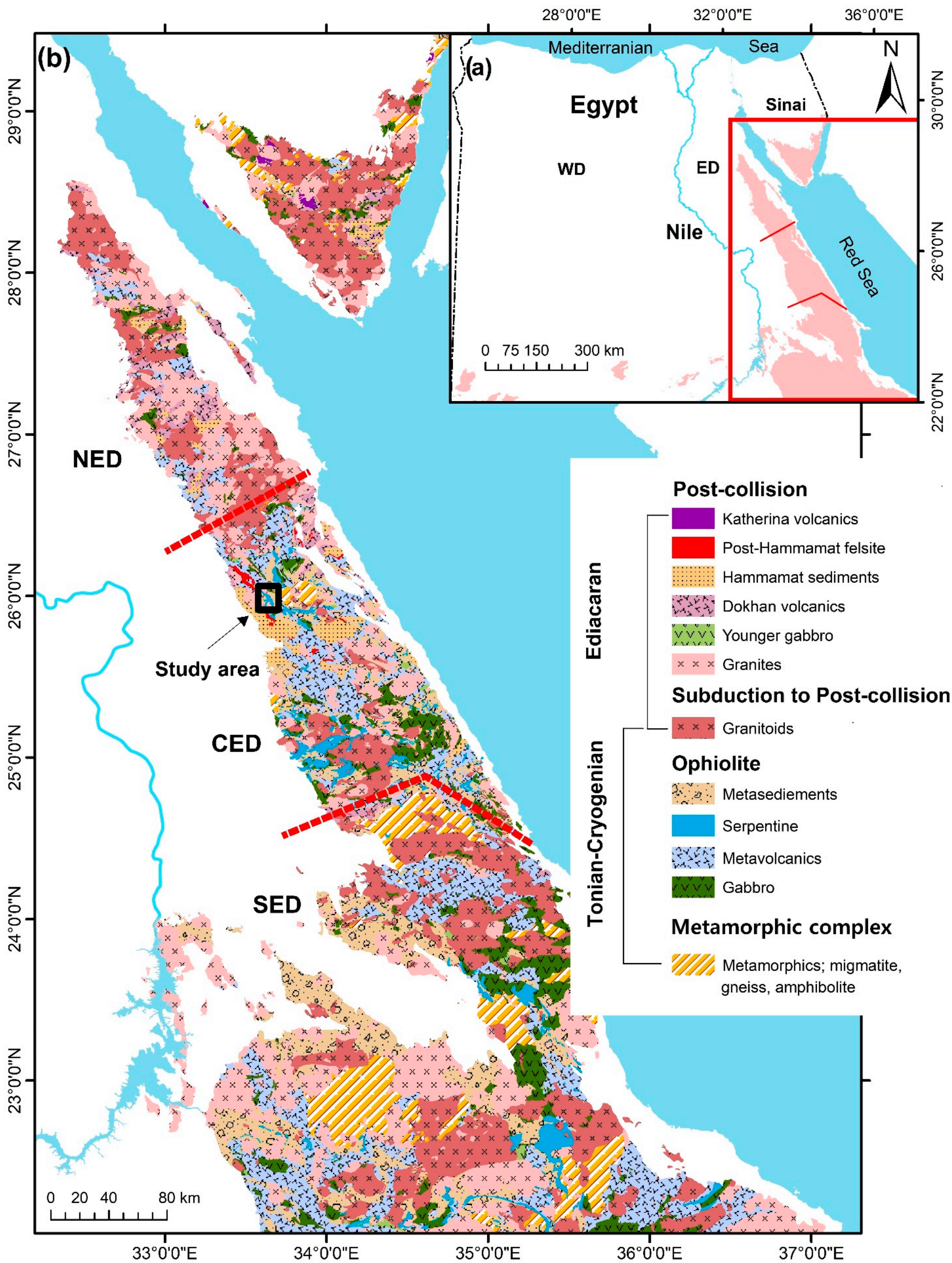

Figure 3. (**a**) distribution of Precambrian rocks in Egypt; (**b**) simplified geologic map of Precambrian rocks in the Easter Desert (ED) and Sinai (modified from [12]).

2. General Geology

The ANS was formed by the amalgamation of the three intra-oceanic island arcs within the Mozambique paleo-ocean during 850–715 Ma [2,3]. The three main intra-oceanic island arcs are as follows from older to younger; (1) the Southern ANS includes Tokar, Barka, Asir, Haya, and Jiddah terranes (~870–740 Ma), (2) the Central ANS includes Gabgaba, Gebeit, and Hijaz terranes (~850–680 Ma), (3) the Northern ANS includes ED and Sinai in Egypt, and Midyan Terran in Saudi Arabia (810–710 Ma) [2,3]. The amalgamation of the three intra-oceanic island arcs is marked by collision along the two main NE-SW directed sutures (blue sutures in Figure 2). Based on current coordinates, the Nakasib-Bi'r Umq suture (NBU) between Southern ANS and Central ANS formed in the south at 780–750 Ma, and the Allaqi-Heiani-Yanbu suture (AHY) between Central ANS and Northern ANS formed in the north at 740–700 Ma [2,3,13,14]. The amalgamated island arcs collided with the Afif-Abas microcontinent in the east along the NNW-SSE directed Nabitah suture, according to present coordinates, during 680–640 Ma, resulting in an enlarged ANS [2,3]. The newly amalgamated ANS has further collided with the eastern margin of the African continent (Sahara metacraton in the north and Congo plate in the southern part) along the NNW-SSE directed Keraf suture during 650–580 Ma [15] (Figure 2). The Indian continent collided with the ANS along the eastern margin of the ANS through the East Africa Orogeny (EAO) [3]. The EAO event resulted from the convergence of West and East Gondwana tectonic plates with the ANS amalgamated arc terranes and Afif-Abas microcontinent in between (Figure 1). The collision occurred among them with the closure of the Mozambique Ocean between West and East Gondwana tectonic plates during 850–550 Ma with a subsequent post-collisional extension [3,13].

Egypt is mainly composed of a Neoproterozoic basement complex consisting of igneous and metamorphic rocks and Phanerozoic sedimentary rocks. The Neoproterozoic rocks are dominant in the ED, the southern part of the Sinai Peninsula, and south of the Western Desert (Figure 3a). The Neoproterozoic rocks in the ED are predominantly composed of ophiolites, gneiss, granitoid, Dokhan volcanics, and Hammamat sediments (Figure 3b). The ED is categorized into three zones based on variations in their geological structures and Neoproterozoic rock types: the North Eastern Desert (NED), Central Eastern Desert (CED), and South Eastern Desert (SED). Ophiolites in the NED are lacking compared to the CED and SED (Figure 3b).

The ophiolites in the ED are distributed irregularly [16], and they occur as either allochthonous blocks or structurally float in a mélange of deep-sea metasediments without clear intrusion relations with the surrounding rocks, indicating that they were tectonically emplaced [17,18]. Ophiolite blocks vary in size from small to mountain size, and complete ophiolite sequences rarely occur in Fawakhir, Ghadir, Geneina, and the Wadi Mubarak areas [17]. Ophiolites consist of serpentinized ultramafic rocks, gabbro to diorite series, sheeted dykes, and massive or pillow basalts [17,19]. The Rb–Sr isochron ages of 850–770 Ma [17] have been reported from ophiolites. The age of the gabbro at Fawakhir was reported as 736 Ma using the zircon U–Pb age dating method [20,21]. The age of ~733 Ma had been reported from diorite and ~700 Ma from rhyolites and andesites in the El-Shadli volcanic province at SED using the zircon U–Pb age dating method [5,6]. The zircon U–Pb age dating on the Diamictite metasediments in the mélange gave 750 Ma [22]. Although these age data indicate the approximate time of the tectonic evolution, the age data is very insufficient for detailed tectonic movement analysis. Besides, the accuracy of age is low. In particular, age data before 800 Ma are very rare and have very low accuracy.

The Fawakhir area is located in the northwest of CED (Figure 3b) and has a typical ophiolite sequence, which consists of serpentinized ultramafic rocks, gabbro, gabbroic diorite, and basaltic rocks and intruded by dacitic and rhyolitic dikes. The Fawakhir ophiolite is surrounded by ophiolitic mélange rocks, especially in the west. Granitic intrusions have structural relationships with the ophiolite rocks; most of the relationships are thrust faults (Figure 4). The ophiolitic mélange consists of allochthons ophiolitic tectonic blocks of serpentinized ultramafic rock, gabbro, gabbroic diorite, diabase, andesite, and basalt in a matrix of deep-ocean metasediments [17]. Ophiolitic rocks are overlain unconformably from south and west by the post-collisional Dokhan volcanic rocks, which are not metamorphosed and have intermediate to silicic whole-rock composition (630–590 Ma) [23–25], and by the Hammamat sediments of clastic molasses-facies (632–590 Ma) [26,27].

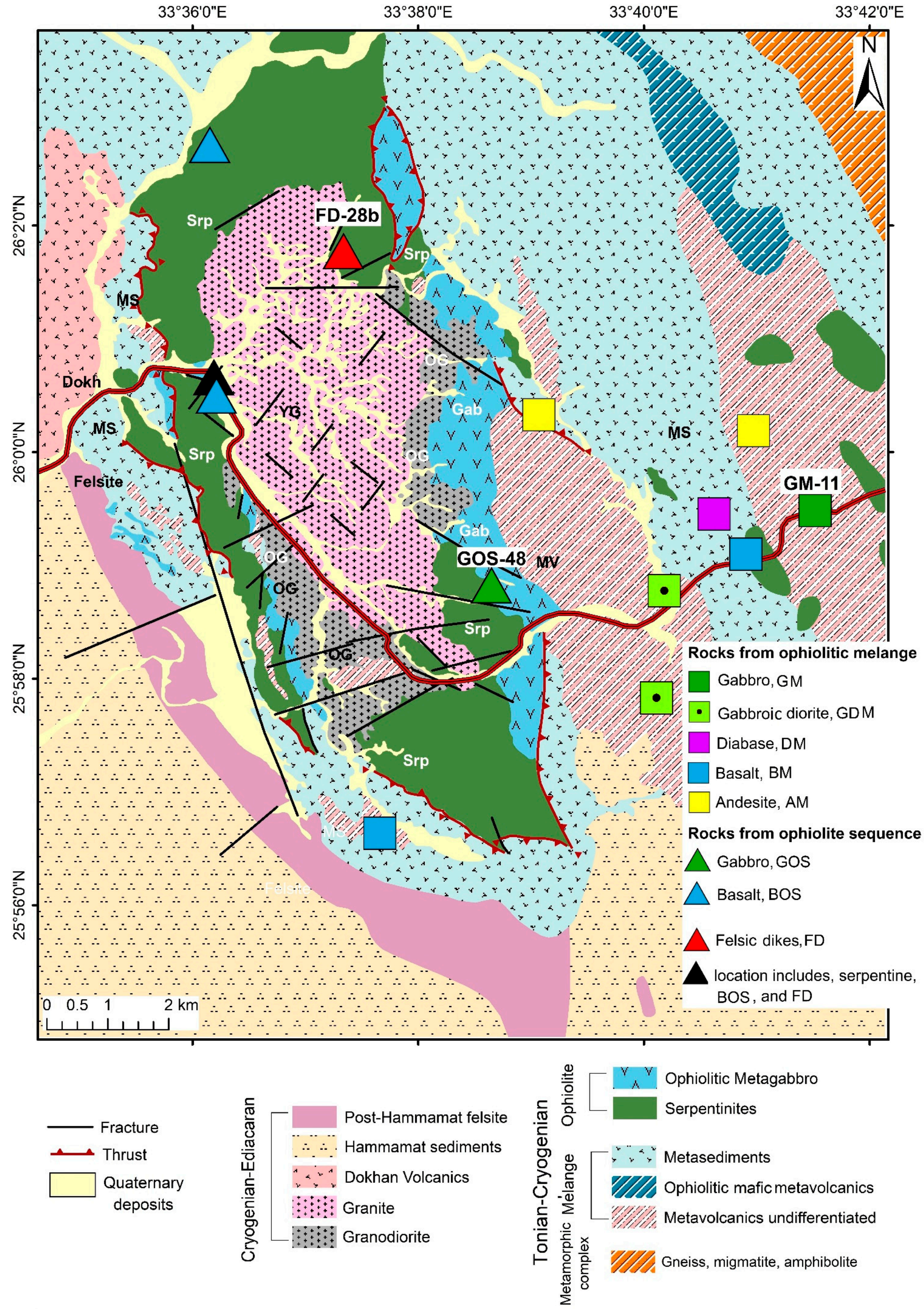

Figure 4. A geologic map of the study area [28]. Fawakhir ophiolite sequence and post-collision related granitoid rocks are located in the west, and the ophiolitic mélange occurs in the east. GM, gabbro from ophiolitic mélange; GDM, gabbroic diorite from ophiolitic mélange; DM, diabase form ophiolitic mélange; BM, basalt from ophiolitic mélange; AM, Andesite from ophiolitic mélange; GOS, gabbro from ophiolite sequence; BOS, basalt from ophiolite sequence; FD, felsic dikes intruding ophiolite sequence. Age dating was carried out on the three samples (GM-11, GOS-48, and FD-28b).

The gabbro, gabbroic diorite, diabase, basalt, and andesite from the ophiolitic mélange locating to the east of the Fawakhir area, and the gabbro, serpentinized ultramafic rocks, and basaltic rocks from the ophiolite sequence, and felsic dikes in the Fawakhir area were collected in this study (Figure 4).

3. Petrography

3.1. Ophiolitic Mélange in the Fawakhir Area

Several types of igneous rocks were collected along the Qift-Quseir road in the ophiolitic mélange located to the east of the Fawakhir area, and one basaltic rock sample was obtained from the ophiolitic mélange located to the south of the Fawakhir area (Figure 4). Hand-specimen photographs of the collected samples are shown in Supplementary Table S1. The collected rocks from the ophiolitic mélange include gabbro, gabbroic diorite, diabase, basalt, and andesite, and occur as tectonic blocks. The gabbro consists mainly of medium-grained plagioclase and amphibole with epidote and opaque minerals as accessory phases (Figure 5a) and shows a phaneritic texture with plagioclase and amphibole. Gabbroic diorites mainly consist of coarse-grained plagioclase, amphiboles, and clinopyroxene (Figure 5b) and are characterized by a phaneritic texture, with an intergrowth of amphibole microcrystals within plagioclase phenocrysts. The diabase is a medium-grained mafic rock consisting of altered plagioclase, amphiboles, opaque minerals, and clinopyroxene (Figure 5c). Volcanic rocks from the ophiolitic mélange are basaltic and andesitic in composition. The basaltic rock consists of fine-to-medium-grained plagioclase, amphiboles, and (occasionally) pyroxene (Figure 5d), while andesite consists mainly of medium-grained quartz, amphiboles, and plagioclase (Figure 5e).

3.2. Ophiolite Sequence in the Fawakhir Area

Two serpentinized ultramafic rocks, one gabbro, three basaltic rocks, and three felsic dikes were collected from the ophiolite sequence in the Fawakhir area (Figure 4, Supplementary Table S1). Two serpentinized ultramafic rocks sampled from the western side of the Fawakhir area are composed of serpentine minerals and Cr-spinel with relic olivine and pyroxene. Most Cr-spinels in the serpentinized ultramafic rocks are changed into magnetite, except for their cores. Relic ortho-pyroxenes are coarse-grained, while relic olivines are medium-grained and also occur as inclusions within pyroxenes that show a poikilitic texture (Figure 6a). The gabbro displays a porphyritic texture in which amphibole phenocrysts occurred, with the matrix consisting of medium-grained plagioclase (Figure 6b). Basaltic rocks from the ophiolite sequence consist of fine-grained amphibole and plagioclase within a glassy matrix, with some samples showing medium- to coarse-grained plagioclase phenocrysts within the glassy matrix (Figure 6c). Felsic dike rocks are volcanic to sub-volcanic rocks and are consisted of quartz, amphibole, and biotite, with minor opaque minerals, and biotite and amphiboles in them occasionally occur as clusters (Figure 6d).

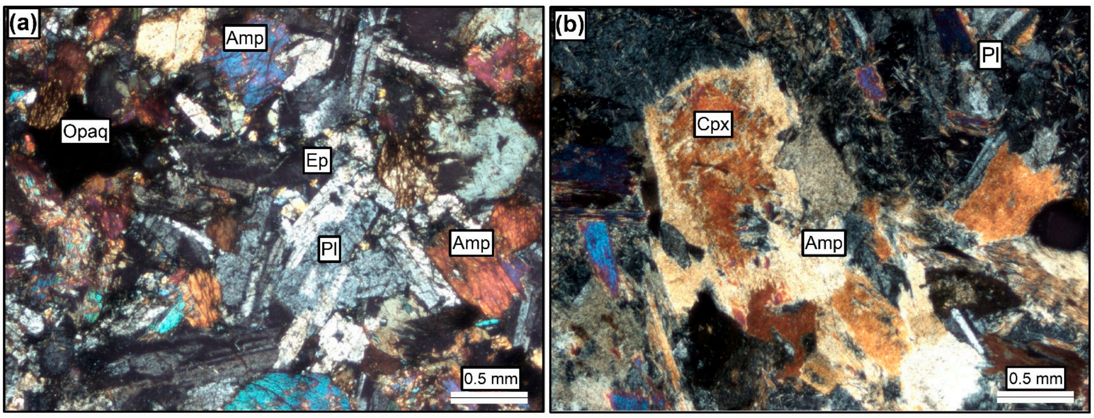

Figure 5. *Cont.*

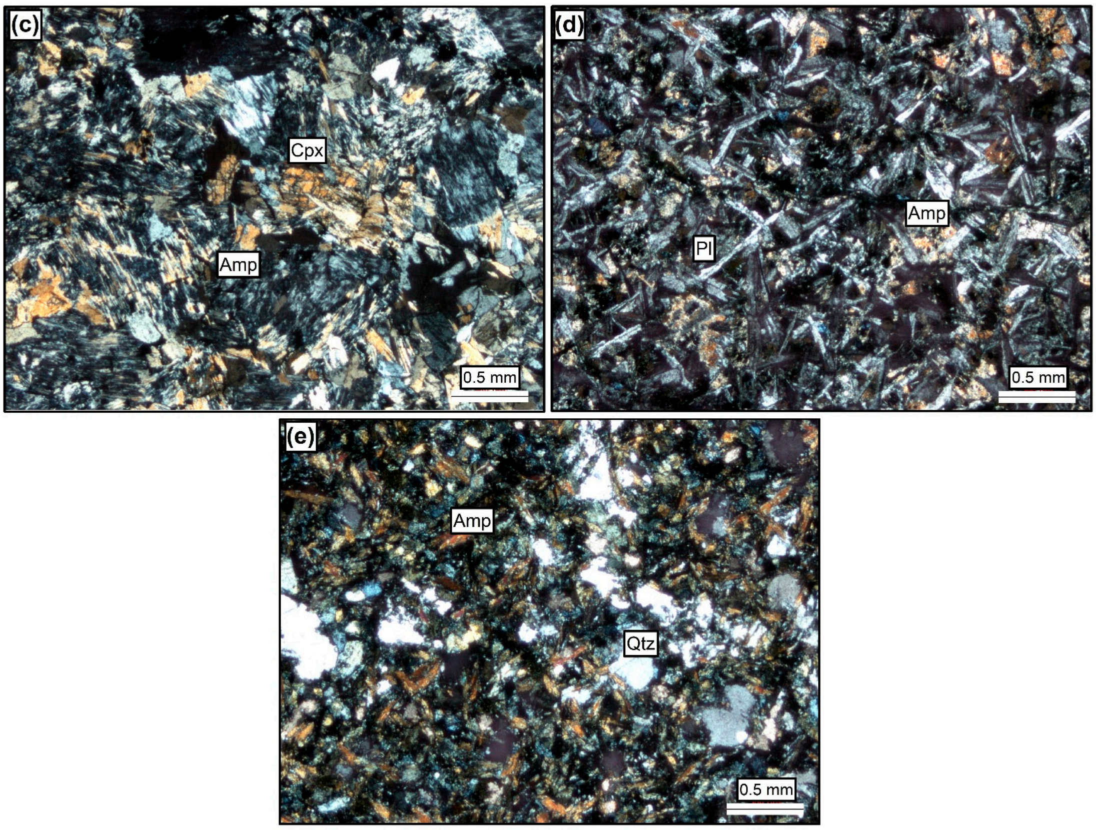

Figure 5. Photomicrographs of rocks in the ophiolitic mélange: (**a**) gabbro (GM-11); (**b**) gabbroic diorite (GDM-46); (**c**) diabase (DM-50E); (**d**) basaltic rocks (BM-40A); (**e**) andesite (AM-59). Pl: plagioclase, Amp: amphiboles, Opaq: opaque minerals, Ep: epidote, Cpx: clinopyroxene, Qtz: quartz.

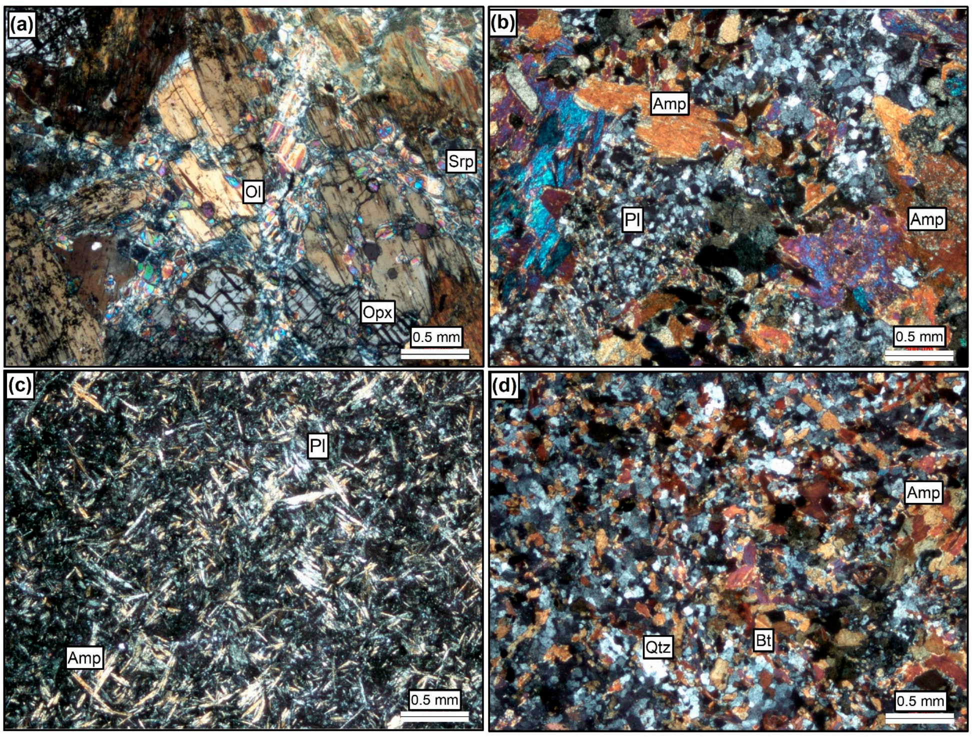

Figure 6. Photomicrographs for rocks in the ophiolite sequence: (**a**) serpentinized ultramafic rock (SOS-2i); (**b**) gabbro (GOS-48); (**c**) basaltic rocks (BOS-25); (**d**) felsic dike rocks (FD-2d). Ol, olivine; Srp: serpentine minerals, Opx: ortho-pyroxene, Pl: plagioclase, Amp: amphiboles, Qtz: quartz, Bt: biotite.

4. Analytical Methods

4.1. Whole-Rock Geochemical Analysis

Two hundred and fifty grams of each sample was crushed to a size of 10-mesh and then pulverized to a size of 200-mesh. Major and trace elements were analyzed by inductively coupled plasma atomic emission spectrometry (ICP-AES; Termo Jarrel Ash ENVIRO II) and inductively coupled plasma mass spectrometry (ICP-MS; Perkin Elmer Optima 3000) at Activation Laboratories, Ltd., Ancaster, ON, Canada. The detailed analytical conditions and methods used are provided in the lithogeochemistry brochures by Activation Laboratories [29], and the detection limits are added to Supplementary Table S4.

4.2. Mineral Chemistry

Major oxides of selected minerals from representative samples were analyzed using a field-emission electron probe microanalyzer (FE-EPMA) at the Gyeongsang National University Instrumental Analysis Center, Jinju, South Korea. The instrument uses 15 kV accelerating voltage, 20 nA beam current, and a probe diameter of 5–10 μm for quantitative analysis. Matrix correction was operated using the conventional atomic number, X-ray absorption, and secondary fluorescence (ZAF) method. The standards used for each oxide are mentioned in Supplementary Table S5. The selected minerals are plagioclase, amphiboles, olivine, pyroxene, and spinel.

4.3. LA–ICP–MS Zircon U–Pb Age Dating and Trace Element Compositional Analysis

Zircon separation, U–Pb age dating, and trace element analysis of zircon from selected representative samples were all performed at Wuhan Sample Solution Analytical Technology Company, Wuhan, China. The zircon U–Pb dating and trace element analyses were operated by the laser ablation–inductively coupled plasma–mass spectrometry (LA–ICP–MS) instrument. Laser ablation was performed using a GeoLasPro laser ablation system that consists of a COMPexPro 102 ArF excimer laser (wavelength of 193 nm and maximum energy of 200 mJ) and a MicroLas optical system. Ion signal intensities were acquired using an Agilent 7900e ICP–MS instrument. Helium was used as a carrier gas to transport the abraded samples and mixed with argon before they entered the ICP–MS. Zircon 91500 and glass standard NIST610 [30,31] were used respectively as external standards for U–Pb dating and trace element calibration. In this study, Plešovice zircon [32] was selected as a consistency standard to check the data quality. The zircon mounts were polished to expose the full width of the majority of the grains to the surface. Each analysis incorporated a background acquisition of approximately 20–30 s followed by 50 s of data acquisition from the sample. The following isotopes were monitored throughout the U–Pb age dating: ^{179}Hf, ^{202}Hg, ^{204}(Pb + Hg), ^{206}Pb, ^{207}Pb, ^{208}Pb, ^{232}Th, and ^{238}U. The age values and isotopic ratio are stated with 2σ precision, while the weighted average is provided at a 95% confidence level. The consistency standard Plešovice zircon shows a Concordia age of 336.57 ± 0.8 (n = 66, MSWD = 0.19) and a weighted mean ^{206}Pb/^{238}U age of 336.56 ± 0.71 Ma (n = 66, MSWD = 0.43), and these results align with the standard values of the Plešovice zircon (337.13 ± 0.37 Ma) [32]. This study employed a ^{206}Pb/^{238}U date for zircons younger than 1000 Ma and a ^{207}Pb/^{206}Pb date for those older than 1000 Ma. The laser spot diameter and frequency of the laser were set to 32 μm and 5 Hz. However, a laser spot diameter of 24 μm was applied for the small zircon grains. Excel-based ICPMSDataCal software was used to perform offline selection and integration of background and analyzed signals, time-drift correction, and quantitative calibration for trace element analysis and U–Pb age dating [33,34]. Concordant data refers to those data points that fall on the Concordia curve within the 2σ uncertainty range. Conversely, data points exhibiting significant discordance (defined as a difference greater than 5% between ^{206}Pb/^{238}U date and ^{207}Pb/^{235}U date) are considered discordant, even if they fall within the error ellipse on the Concordia curve. The detailed sample preparation and analysis procedures for U–Pb dating and trace element analysis of zircon were described in previous reports [35]. The Concordia diagrams and weighted mean calculations were generated using Isoplot/Ex4.15 and an Excel-based macro [36].

5. Results

5.1. Rocks in the Ophiolitic Mélange

5.1.1. U–Pb Zircon Age Dating and Trace Element Composition of Zircons

Zircons from Gabbro (GM-11) from the ophiolitic mélange were analyzed for U–Pb dating (Figure 7a–c; Supplementary Table S2). The zircon grains range from 37.6–124.6 μm in length and 22.2–96.6 μm in width. Zircon grains commonly show oscillatory zoning, which is a typical characteristic for igneous zircon, and have very thin outer bright rims, which may form during metamorphism but are too thin to be analyzed (Figure 7a). Twenty-one analyzed data points are plotted on the Wetherill Concordia diagram, giving an upper intercept age of 856 ± 20 Ma. The Concordia age obtained from three concordant zircons is 816.5 ± 7.4 Ma (*n* = 3, MSWD = 0.14), which is more accurate than the upper intercept age and represents the timing of magmatism (Figure 7b).

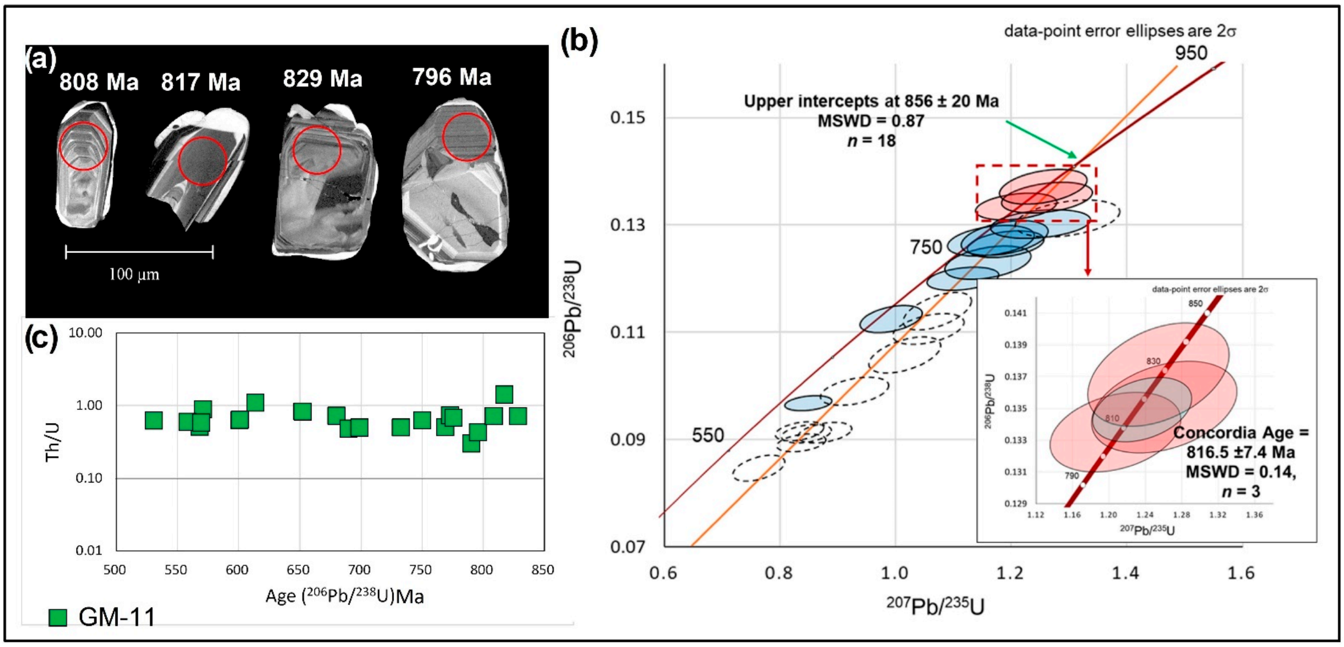

Figure 7. Zircon U–Pb age dating results of the gabbro from the ophiolitic mélange (GM-11): (**a**) CL image of representative zircon grains with $^{206}Pb/^{238}U$ dates; (**b**) Concordia-plot for all measured zircon data using 2σ error range with the Concordia-age. Red ellipses are concordant data used to calculate Concordia age, blue ellipses with younger ages are also concordant but affected by Pb-loss, and dashed ellipses indicate discordant data; (**c**) Zircons plotted in the Th/U vs. $^{206}Pb/^{238}U$ age diagram.

The trace element composition of all zircons from gabbro (GM-11) was plotted on tectonic discrimination diagrams for zircon (Figure 8, Supplementary Table S3). The zircons of gabbro have Th/U ratios of 0.31–1.47 (Figure 7c), Nb/Hf ratios of 0.00015–0.00112, Th/Nb ratios of 38–254, and Hf/Th ratios of 9–152. They are typically plotted within the arc tectonic setting fields (Figure 8a,b). The gabbro has Y and Hf contents of 243–2996 ppm and 7626–11552 ppm, respectively, with U/Yb ratios of 0.62–3.08. These results are consistent with the zircons formed in the continental arc tectonic setting (Figure 8c,d).

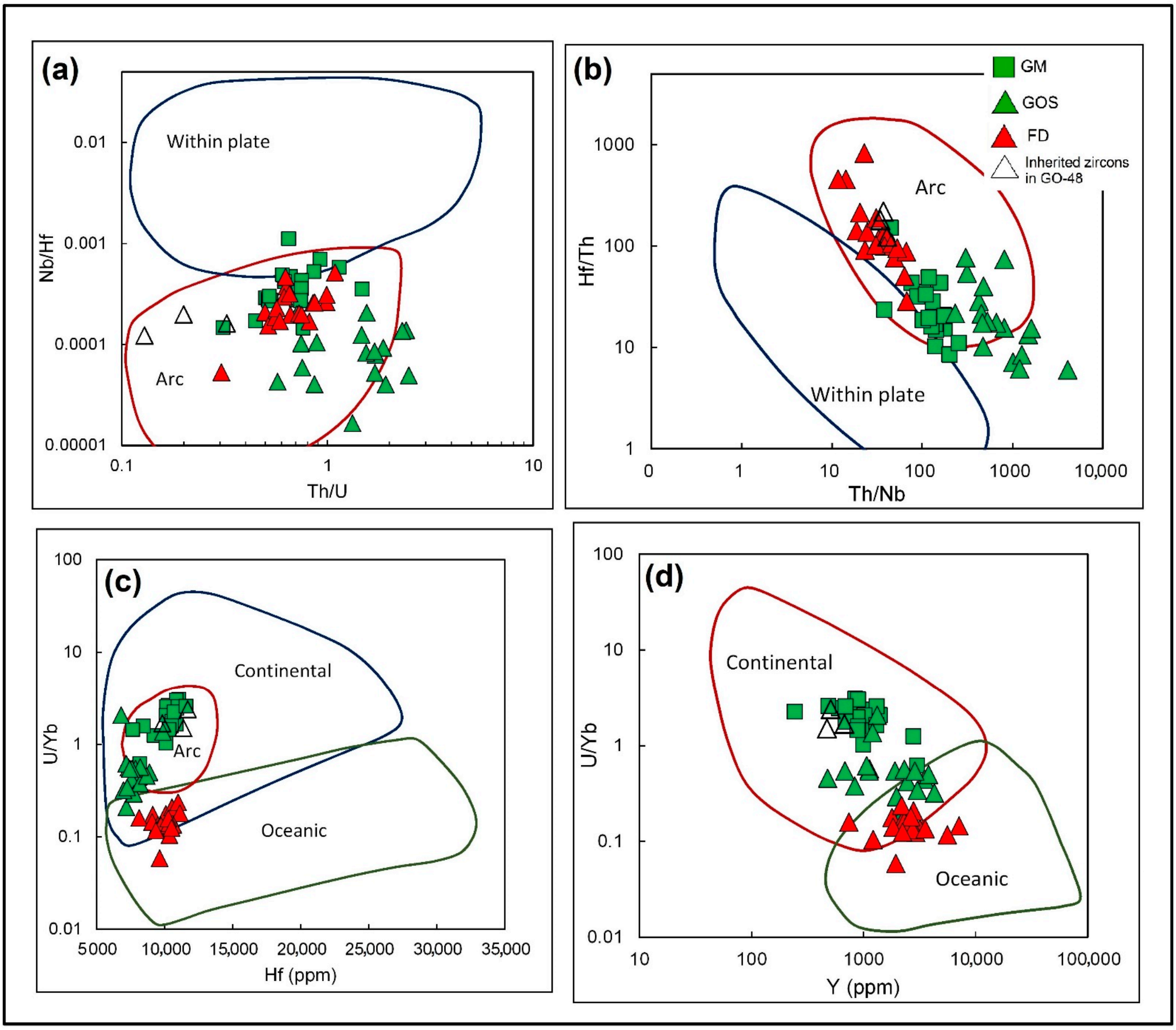

Figure 8. Plot of zircons from the rocks in the ophiolitic mélange and ophiolite sequence and from felsic dike rocks (GM-11, G-48, and FD-28b) in the Th/U vs. Nb/Hf and Th/Nb vs. Hf/Th tectonic discrimination diagrams [37] (**a**,**b**); and in the Hf vs. U/Yb and Y vs. U/Yb tectonic discrimination diagrams [38] (**c**,**d**). The arc field in (**c**) is from [39].

5.1.2. Whole-Rock Geochemical Analysis and Tectonic Settings

Four plutonic and six volcanic rocks were collected from seven distinct locations within the ophiolitic mélange (Figure 4). They show mafic to intermediate compositions (Supplementary Table S4). Based on the total alkali (Na_2O + K_2O) and silica (SiO_2) content [40], they are classified into gabbro, gabbroic diorite, basalt, trachy-basalt, and basaltic andesite (Figure 9).

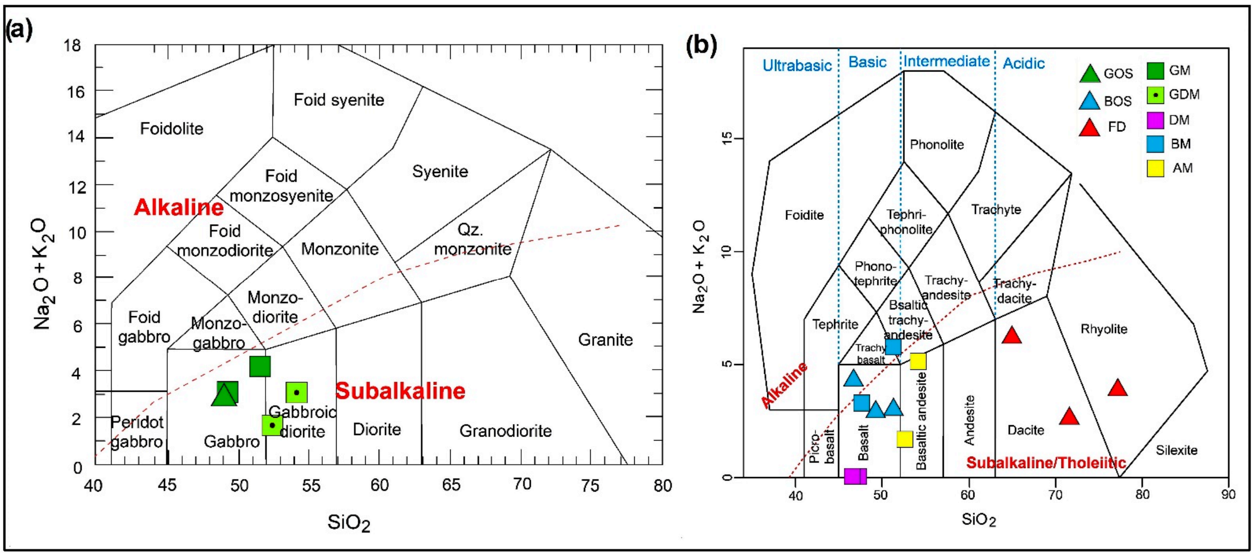

Figure 9. Plot of plutonic rocks (**a**) and volcanic rocks (**b**) on the TAS classification diagram [40]. The line between alkaline and sub-alkaline fields was fitted by [41].

Both gabbro and volcanic rocks, including basaltic and basaltic-andesite rocks, are plotted in the island arc tectonic setting fields in the Ti vs. V [42], Y vs. Cr [43,44], and Ti/40-Si/100-Sr [45] tectonic discrimination diagrams (Figure 10a–c). Meanwhile, gabbroic diorite and diabase, due to their very low Y and Ti content, are plotted in the boninite field of the Ti vs. V and Y vs. Cr diagrams (Figure 10a,b).

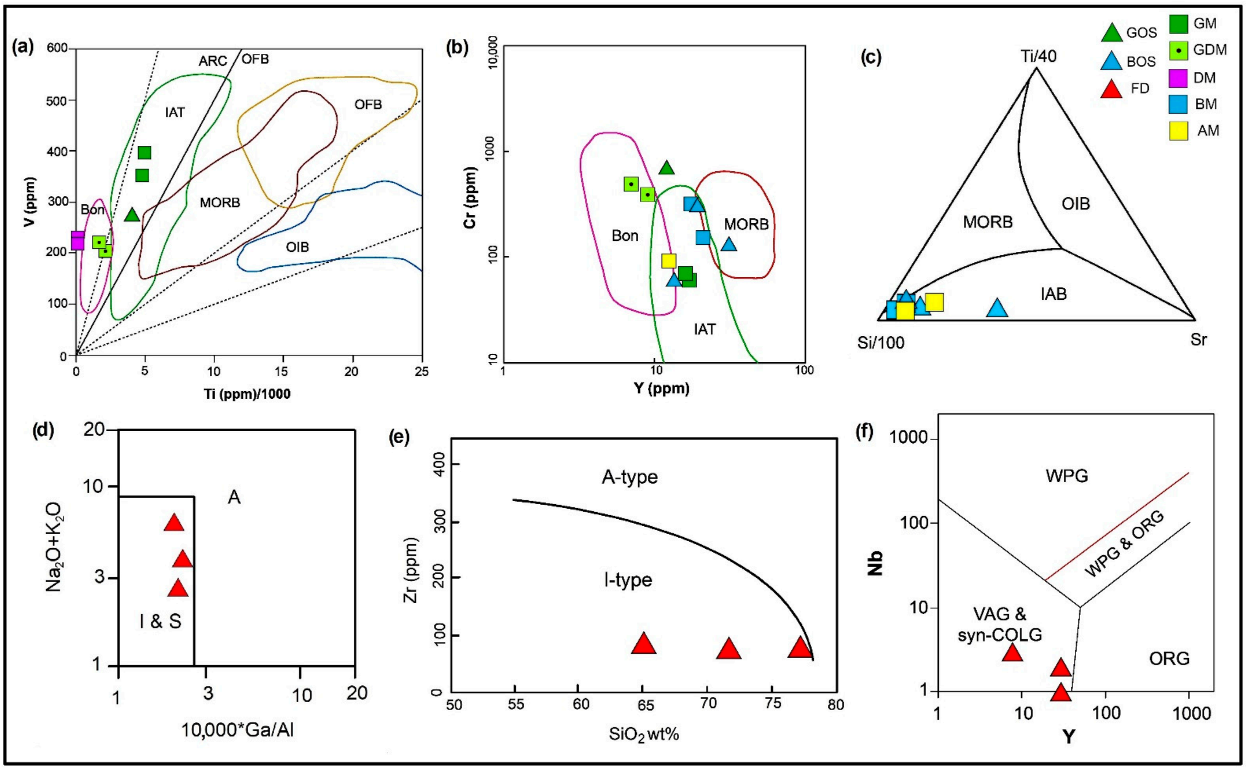

Figure 10. Plot of mafic rocks in (**a**) the Ti vs. V tectonic discrimination diagram [42], (**b**) the Y vs. Cr diagram [43,44], and (**c**) the Ti/40-Si/100-Sr diagram [45]. Plot of felsic dike rocks in (**d**) the 10,000 Ga/Al vs. $Na_2O + K_2O$ tectonic discrimination diagram [46], (**e**) the SiO_2 vs. Zr diagram (for discriminating I-type from A-type rocks) [47], and (**f**) the Y vs. Nb diagram [48].

The content of rare earth elements (REEs) and trace elements indicates that gabbro, gabbroic diorite, and one of basaltic-andesite are more depleted than those of MORB in both light REEs (LREEs) and heavy REEs (HREEs) (Figure 11a,b; Supplementary Table S4), while the other basaltic-andesites are enriched in the LREEs and depleted in the HREEs similar to OIB. One basaltic rock shows a REE pattern similar to that of E-MORB. The Nb and Ta contents of the gabbro, gabbroic diorite, and one basaltic-andesite rock are beneath the detection limit, and the other basaltic andesites show Nb and Ta negative troughs in a Primitive mantle normalized multi-element diagram (Figure 11a,b). E-MORB, like basaltic rock, in contrast, does not show an Nb and Ta trough. The REE content of diabases is very depleted and under the detection limit.

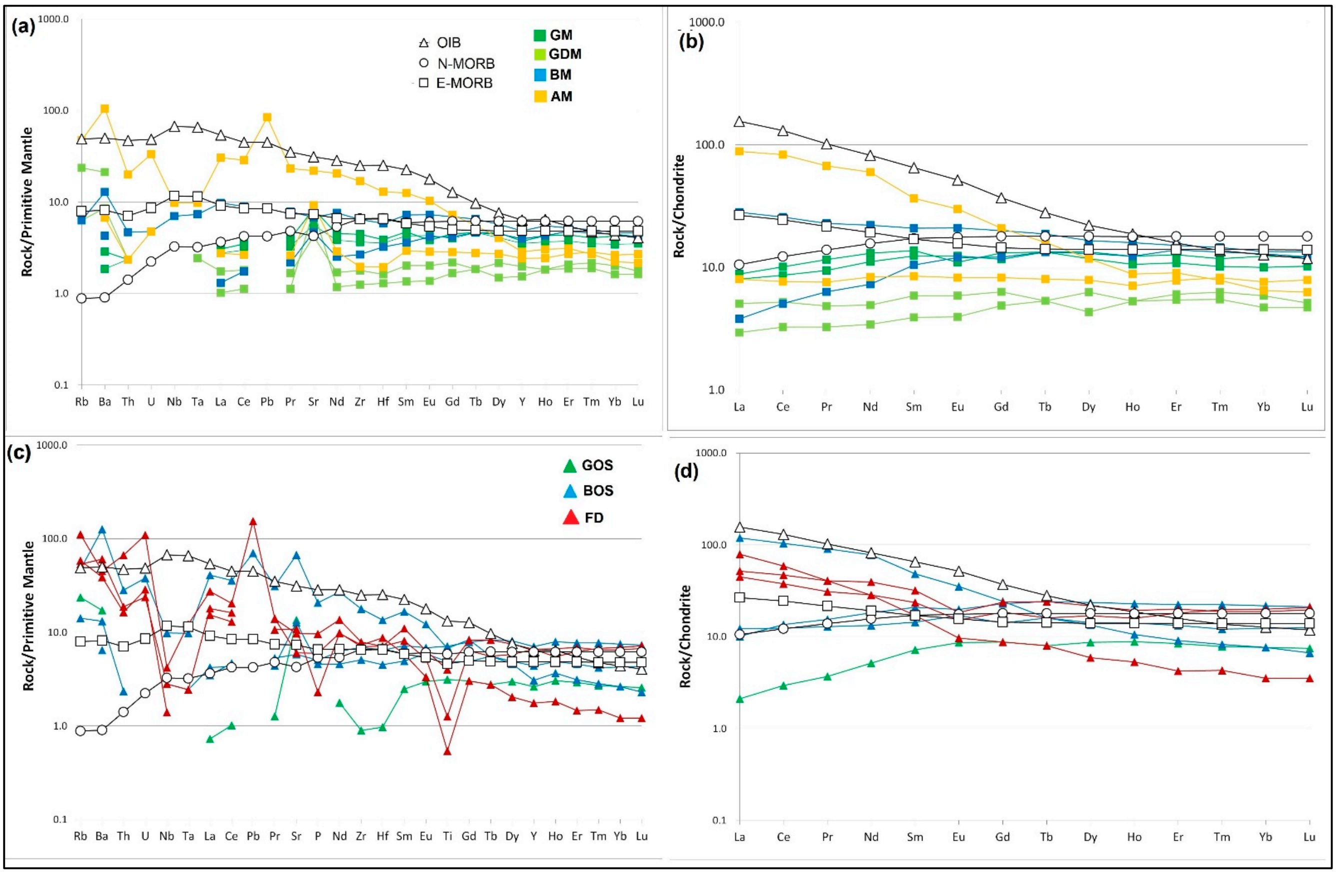

Figure 11. Plot of rocks from the ophiolitic mélange and ophiolite sequence in the spider diagrams normalized by Primitive mantle (**a**,**c**), and in the chondrite-normalized REE diagrams (**b**,**d**). The values of the Primitive mantle and chondrite used for normalization and the E-MORB, N-MORB, and OIB values are from [49].

5.2. Rocks in the Ophiolite Sequence and Felsic Dikes (742–723 Ma)

5.2.1. U–Pb Zircon Age Dating and Trace Element Composition of Zircons

The gabbro (GOS-48) from the ophiolite sequence and felsic dike (FD-28b) were selected for zircon U–Pb age dating (Supplementary Table S2). Zircon grains obtained from gabbro (GOS-48) are euhedral and elongated. Their length varied between 38.2–179.4 µm and their width between 23.7–89.1 µm. The zircon grains frequently show oscillatory zoning and have an outer bright rim that is visible in the CL image, indicating that they are of igneous origin with a metamorphic overgrowth rim (Figure 12a). The outer rims are too thin to be analyzed. All 22 analyzed points were measured by a laser spot diameter of 24 µm. The zircons in gabbro show two Neoproterozoic age clusters (Figure 12b). The older cluster gives a Concordia age of 742.7 ± 4.9 Ma (n = 10, MSWD = 0.9), while the younger cluster shows a Concordia age of 708.0 ± 7 Ma (n = 5, MSWD = 0.035) (Figure 12b). The older Concordia age was obtained from the zircons with banded zoning, indicating the timing of magmatism, while the younger Concordia age was obtained from the zircons with weak zoning, representing Pb-loss attributable to subsequent tectono-thermal events, which may form the bright crummy rim (Figure 12a). All analyzed zircons show ^{238}U and ^{232}Th contents of 91.5–1353 ppm and 53.4–1208 ppm, respectively, with a Th/U ratio between 0.13 and 2.48, further indicating an igneous origin together with oscillatory zoning (Figure 12a,c). Three inherited zircons show apparent $^{207}Pb/^{206}Pb$ dates of 2154, 2109, and 2420 Ma (Figure 12b).

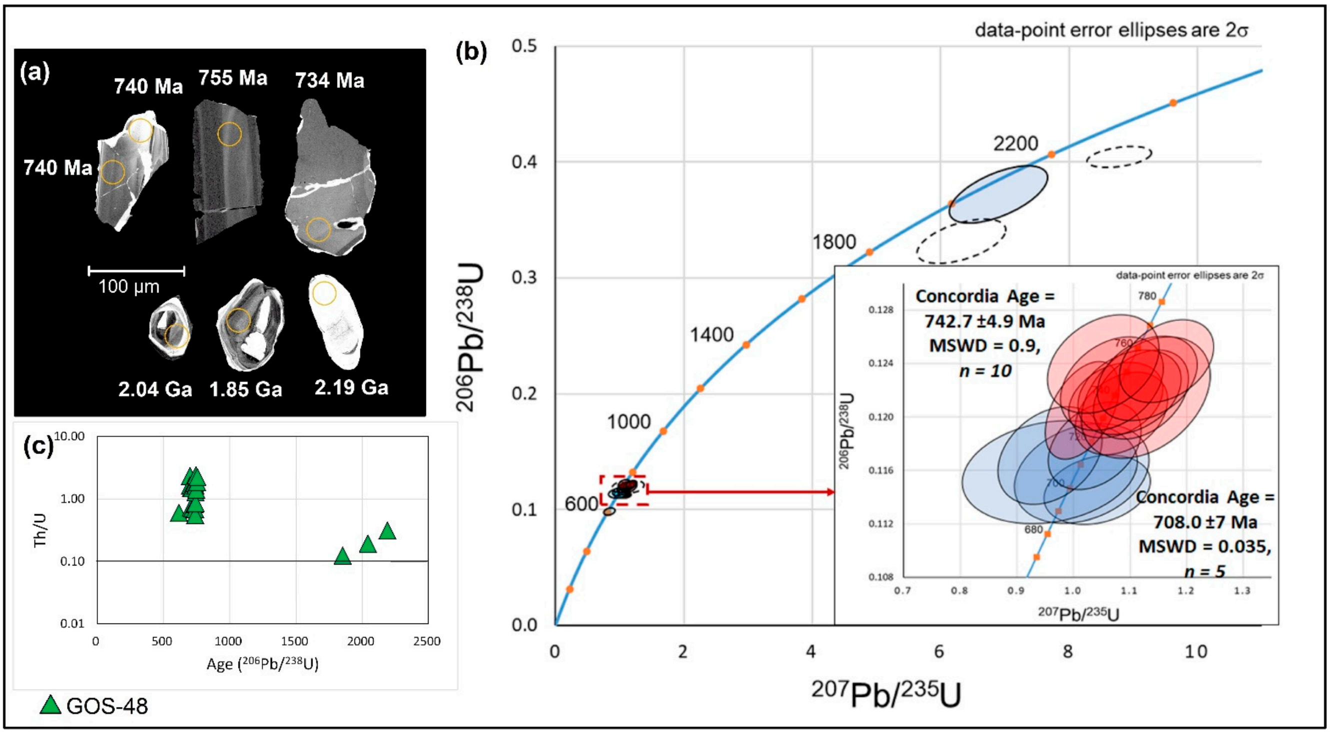

Figure 12. Zircon U–Pb age dating results of the gabbro from the ophiolite sequence (GOS-48): (**a**) CL image of representative zircon grains with $^{206}Pb/^{238}U$ ages for three Neoproterozoic grains and $^{207}Pb/^{206}Pb$ ages for three inherited Paleoproterozoic grains; (**b**) Concordia-plot of all measured zircon data using 2σ error value. Red ellipses are concordant data used for Concordia age calculation (742 Ma) which indicate the intrusion age, and the blue ellipses represent the dates that may reflect the Pb loss effect; (**c**) Zircons plotted in the Th/U ratio vs. age diagram.

The felsic dike sample (FD-28b) contains euhedral zircon grains varying in length between 22.5–110.0 μm and in width between 13.6–59.5 μm (Figure 13a). They show clear oscillatory zoning, with a bright outer rim that is visible on the CL images (Figure 13a). Twenty analyzed points were measured by a laser spot with a diameter of 24 μm, giving 17 concordant measured points. The U–Pb dating results show a clear cluster that yields a Concordia age of 723.5 ± 6.6 Ma (n = 16, MSWD = 0.13) (Figure 13b). One analysis gave the younger apparent date of ~658 Ma, which may have been caused by a possible Pb loss during a later tectono-thermal event that formed the bright rim. The ^{238}U and ^{232}Th contents for all measured zircons are 39.0–655 ppm and 12.4–184 ppm, respectively, and the Th/U ratios of zircons yield 0.25–1.05, indicating an igneous origin along with their oscillatory zoned microtexture (Figure 13c).

Zircon trace element compositions of both analyzed samples were plotted on tectonic discrimination diagrams for zircon (Figure 8; Supplementary Table S3). The Neoproterozoic zircons from GOS-48 and FD-28b have Th/U ratios of 0.57–2.48 and 0.30–1.09, Nb/Hf ratios of 0.00002–0.00021 and 0.00005–0.00052, Th/Nb ratios of 232–4111 and 12–68, and Hf/Th ratios of 6–77 and 29–827, respectively. These are mostly plotted within the fields of an arc tectonic setting (Figure 8a,b). They have Y contents of 479–4300 ppm and 742–7143 ppm, and Hf contents of 6806–9867 ppm and 8126–11112 ppm, respectively. They have U/Yb ratios of 0.21–2.07, 0.06–0.24, and Nb/Yb ratios of 0.000421–0.002216 and 0.001589–0.005393, respectively (Figure 8c,d). The Neoproterozoic zircons from the gabbro GOS-48 plotted in the continental-arc tectonic settings field, while the zircons from the felsic dike sample FD-28b plot in the overlapped fields between the continental and oceanic tectonic setting fields, indicating their effect by backarc basin opening within the continental arc. In contrast, the three Paleoproterozoic inherited zircon grains from the sample GOS-48 give Th/U ratios of 0.13–0.32, Nb/Hf ratios of 0.00012–0.00020, Th/Nb ratios of 34–41, and Hf/Th ratios of 124–219, and are plotted in the arc tectonic setting (Figure 8a,b). Their Y content of 471–677 ppm, Hf content of 9816–11688 ppm, U/Yb ratios of 1.5–2.4, and Nb/Yb ratios of 0.007959–0.01372 represent a continental-arc tectonic setting (black points in Figure 8c,d).

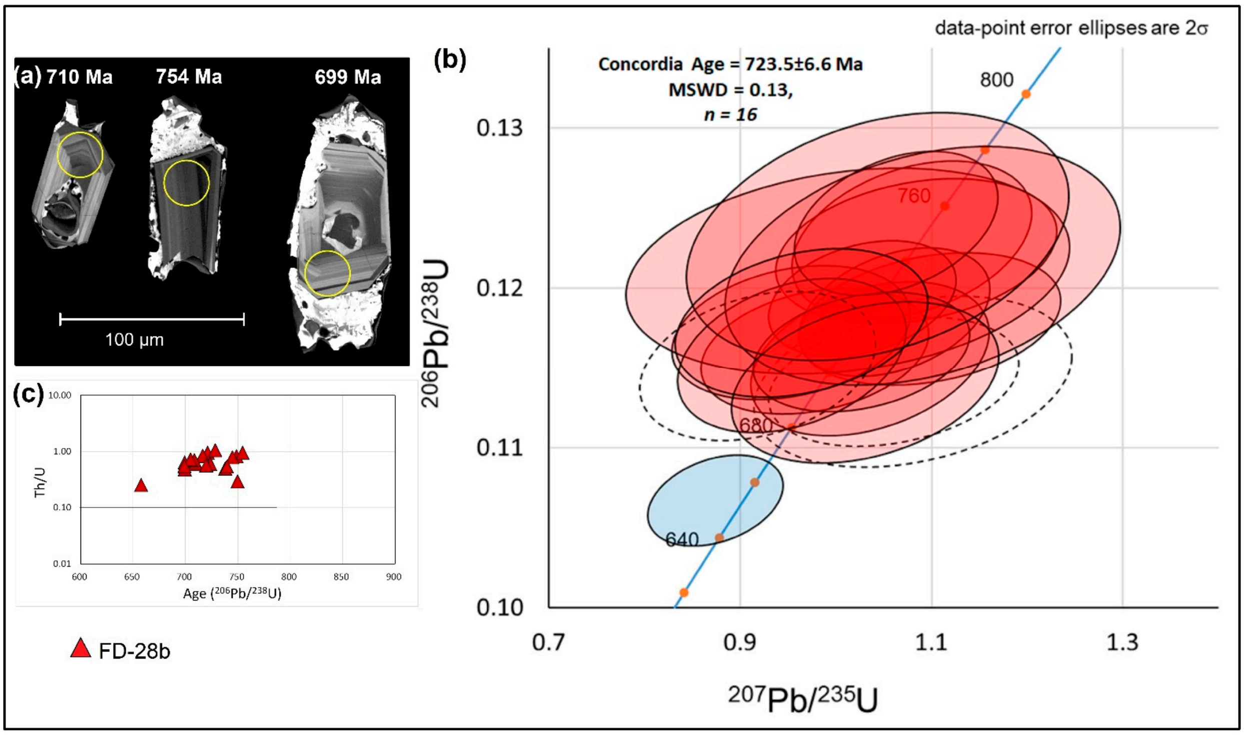

Figure 13. Zircon U–Pb age dating results of the felsic dike rock in the ophiolitic sequence (FD-28b): (**a**) CL image of representative zircon grains with $^{206}Pb/^{238}U$ dates; (**b**) Concordia-plot for all measured zircon data using 2σ error value. Red ellipses are concordant data used for Concordia age calculation (723 Ma) which indicate the intrusion age; the blue ellipse represents the apparent age as affected by Pb loss, and the dashed ellipses indicate discordant data; (**c**) zircons plotted in the Th/U ratio vs. $^{206}Pb/^{238}U$ date diagram.

5.2.2. Whole-Rock Geochemical Analysis and Tectonic Settings

Nine samples were collected from five different localities in the ophiolite sequence (Figure 4). The samples include ultramafic to mafic plutonic rocks, mafic volcanic rocks, and felsic dikes. On the SiO_2 and $Na_2O + K_2O$ classification diagram, these are classified as serpentinized ultramafic rock, gabbro, basalt, dacite, and rhyolite (Figure 9).

Under the tectonic discrimination diagrams [42–45], both gabbro and basaltic rocks are plotted in the typical island arc tectonic setting fields (Figure 10a–c). In the Zr vs. SiO_2 diagram [46,47], the felsic dike samples have an I-type affinity based on their major and trace elements (Figure 10d,e). They plotted within the volcanic-arc fields in the Nb vs. Y tectonic discrimination diagram [48] (Figure 10f).

In the primitive mantle normalized multi-elements and chondrite normalized REE diagrams, the gabbro shows a more depleted pattern than MORB for the content of most trace elements and REEs, except for Rb, Ba, and Sr (Figure 11c,d; Supplementary Table S4). Two basalt samples show an REE pattern similar to N-MORB and are depleted in U, Nb, Ta, and Pb, while the third basalt sample shows an REE pattern similar to OIB with negative anomalies of Nb and Ta in their trace element pattern (Figure 11c,d). Serpentinized ultramafic rocks are highly depleted in trace elements and REE contents, which are mostly under the detection limit of the instrument. In the primitive mantle normalized multi-elements diagram, felsic dike rocks are plotted between OIB and MORB, with negative anomalies of Nb, Ta, and a very low Pb content, except for one sample that shows a positive Pb anomaly (Figure 11c). The felsic dikes are plotted between OIB and MORB trends in the REE diagram, and one of them is more depleted in middle REEs (MREEs) and HREEs than MORB (Figure 11d).

Serpentinized ultramafic rocks are classified as harzburgite due to the absence of clinopyroxene and the abundance of olivine and orthopyroxene. The spinels in them contain low Al_2O_3 and CaO (13.63–14.76 wt% and 8.41–11.35 wt%, respectively) and are plotted as forearc peridotite on the Al_2O_3 vs. SiO_2/MgO diagram, suggesting that they were formed under a forearc tectonic setting (Figure 14a). The composition of the spinels falls within the depleted peridotite in the TiO_2 vs. Cr# diagram (Figure 14b) and on the suprasubduction zone tectonic setting in the Al_2O_3 vs. TiO_2 diagram (Figure 14c). Also, the forearc character of the spinels is confirmed by the high Cr# and Mg# (Figure 14d,e). The compositions of the spinel and olivine fall within the field, which indicates their formation in the suprasubduction zone with a partial melting degree of ~30%–40% under a pressure of ~5 kbar (Figure 14f).

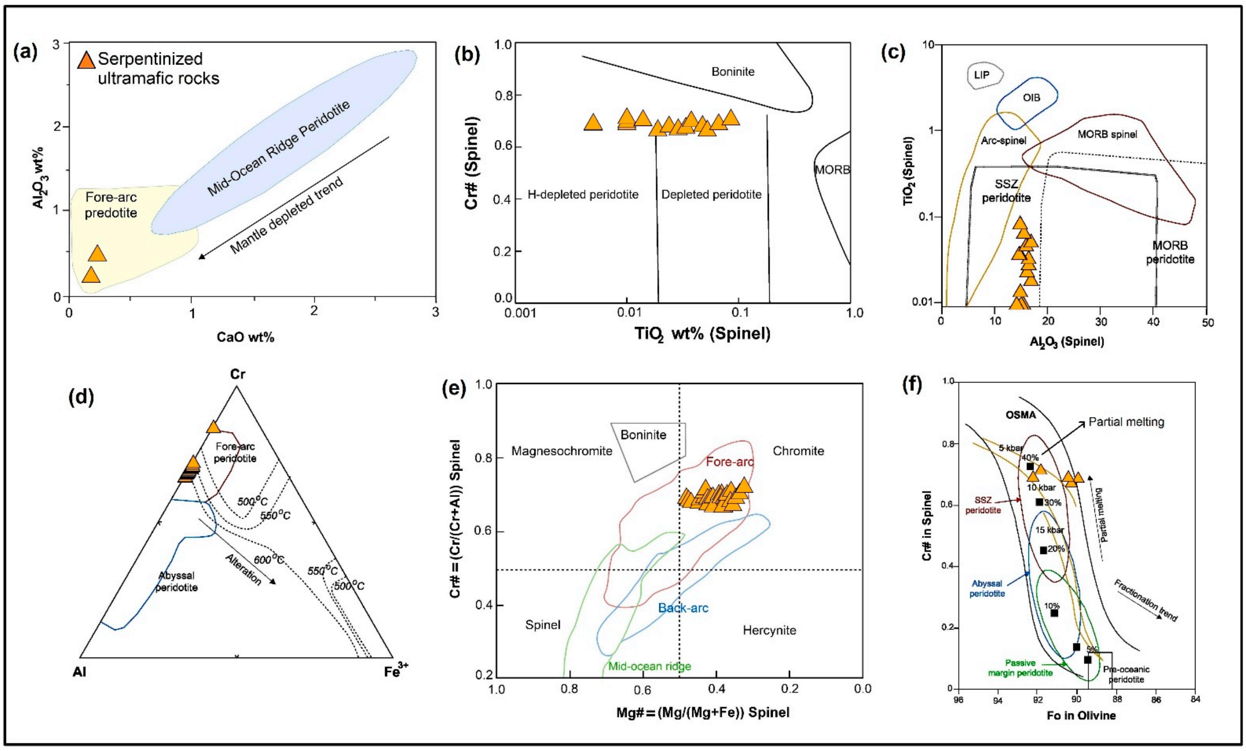

Figure 14. (**a**) Plot of the whole-rock composition of the serpentinized ultramafic rocks in the CaO vs. Al_2O_3 wt% tectonic discrimination diagrams [50]. Plot of compositions of spinels from the serpentinized ultramafic rocks in the (**b**) TiO_2 vs. Cr# diagram [51]; (**c**) Al_2O_3 vs. TiO_2 diagram [52]; (**d**) Cr-Al-Fe^{3+} ternary diagram [53], forearc and abyssal peridotites fields are from [50,54], respectively; and (**e**) Mg# vs. Cr# diagram [55]. (**f**) Plot of spinel and olivine compositions in the Cr# of spinel vs. Fo of coexisting olivine diagram [53]. Cr# = molar Cr/(Cr + Al), Fo = 100 × Mg/(Mg + Fe^{2+}), OSMA: the olivine-spinel mantle array.

5.2.3. Mineral Chemistry

The chemical composition of the orthopyroxene, olivine, and spinel in serpentinized ultramafic rocks was analyzed using FE-EPMA (Supplementary Table S5). Orthopyroxenes are classified as enstatite on the pyroxene classification diagram [56,57] (Figure 15a) and have 57.2–62.0 wt% SiO_2, 29.0–36.8 wt% MgO, 1.2–5.9 wt% FeO, 0.13–0.74 wt% Al_2O_3, and 0.050–0.146 wt% Cr_2O_3. Olivines are forsterite in their composition with SiO_2 of 40.5–41.4 wt%, MgO of 48.6–50.8 wt%, FeO of 7.6–9.7 wt%, Mg# of 90–92, and Al_2O_3 of 0.012–0.032 wt%. Spinel grains are chromite (Figure 15b), which have Cr_2O_3 of 51.00–60.30 wt%, FeO of 20.12–26.67 wt%, Al_2O_3 of 6.88–16.94 wt%, MgO of 5.26–10.46 wt%, Cr# of 67.00–85.00, and Mg# of 26.00–48.00.

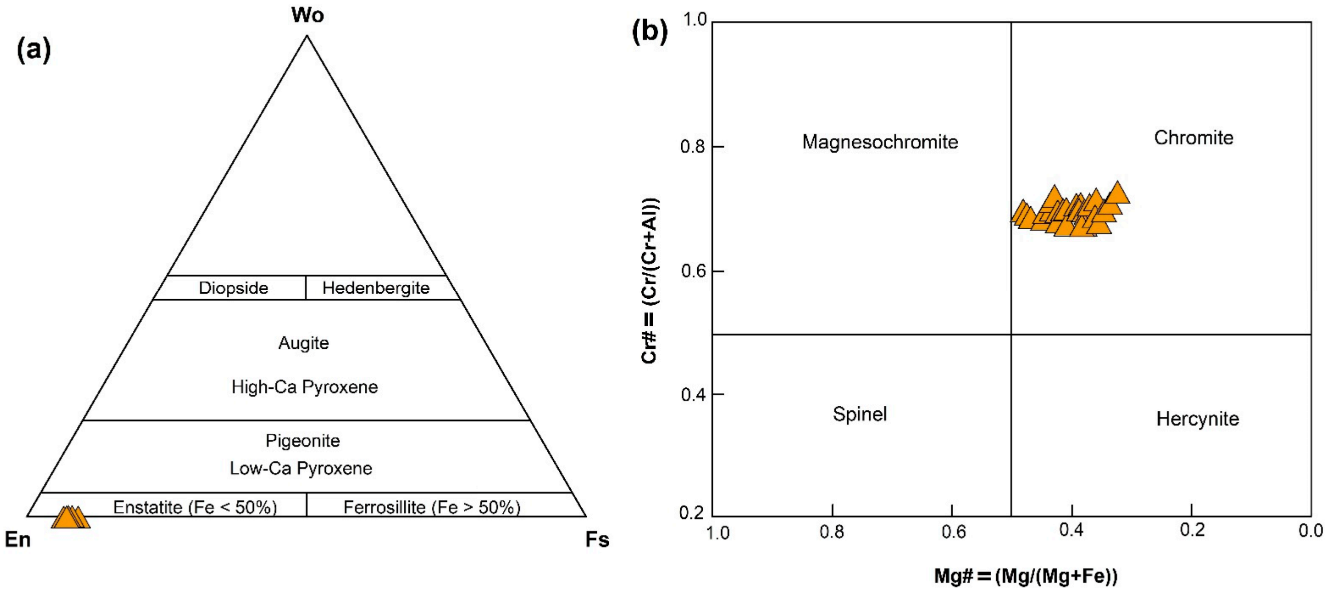

Figure 15. (**a**) Plot of pyroxene in the classification diagram [56,57]; (**b**) Plot of spinel in the classification diagram [58].

6. Discussion

6.1. Petrogenesis and Tectonic Evolution of Tectonic Blocks in the Ophiolitic Mélange (~816 Ma)

Ophiolitic mélange surrounds the Fawakhir area. This includes abundant tectonic blocks consisting of ultramafic to intermediate igneous rocks within the matrix, which is composed of turbidite sequence and deep-sea flysch. Among them, gabbroic diorite and diabase are depleted in Ti and Y, showing the geochemical characteristics of boninite (Figure 10a,b), which is commonly generated during the initiation of subduction as an intra-oceanic island arc [59–62]. Their boninitic character is also supported by the highly depleted nature of their REE contents and high Mg [63,64]. The sampled gabbro shows an intrusion age of 816 Ma (Figure 7b). The other tectonic blocks including gabbro from the ophiolitic mélange display geochemical signatures similar to an island arc tholeiite in the V (ppm) vs. Ti (ppm)/1000 and Cr (ppm) vs. Y (ppm) tectonic discrimination diagrams (Figure 10a,b). The trace element compositions of zircons from the gabbro represent continental arc origin (Figure 8). These data suggest that the study area was a thin continental island arc separated from an older continent. Generally, the continental crust can be distinguished from the oceanic crust by its more evolved and differentiated nature in a whole-rock composition [65]. If the continental crust is thin, i.e., less than 35–30 km thick, its whole-rock geochemical composition will be rather similar to island arcs [66,67], such as the case of continental arcs at the southwestern margin of the South American continent [67]. Likewise, it has been claimed that the Egyptian basement complex was initiated from the continental nucleus of the Archean age in southwestern Egypt and grew by adding the Neoproterozoic juvenile crust [17], which supports our interpretation.

In a chondrite-normalized REE diagram, whole-rock chemical data of the tectonic blocks from the ophiolitic mélange often show a nearly flat pattern similar to those of E- and N-MORB, except for one andesite rock sample that shows a systematic increasing pattern toward LREEs similar to OIB (Figure 11a,b). The Nb and Ta contents in the tectonic blocks are lower than the detection limit, and one andesite rock shows an Nb–Ta negative trough, indicating their arc origin as confirmed by whole-rock chemical composition.

In light of all of the geochemical data presented above, we suggest that the tectonic blocks in the ophiolitic mélange formed in an island arc tectonic setting within the thin-continental margin associated with the backarc opening during 816 Ma (Figure 16a,b). Although arc-related activities in the ED older than 800 Ma have been proposed in previous studies, no clear age data has been reported therein. This study clearly supports the existence of an 816 Ma island arc in the CED. Furthermore, the presence of boninitic diabase indicates that the subduction had started in the Fawakhir area before ~816 Ma and may have continued until ~740–700 Ma when the collision occurred along the AHY suture in the southern margin of the ED [2,3] (see Figure 2).

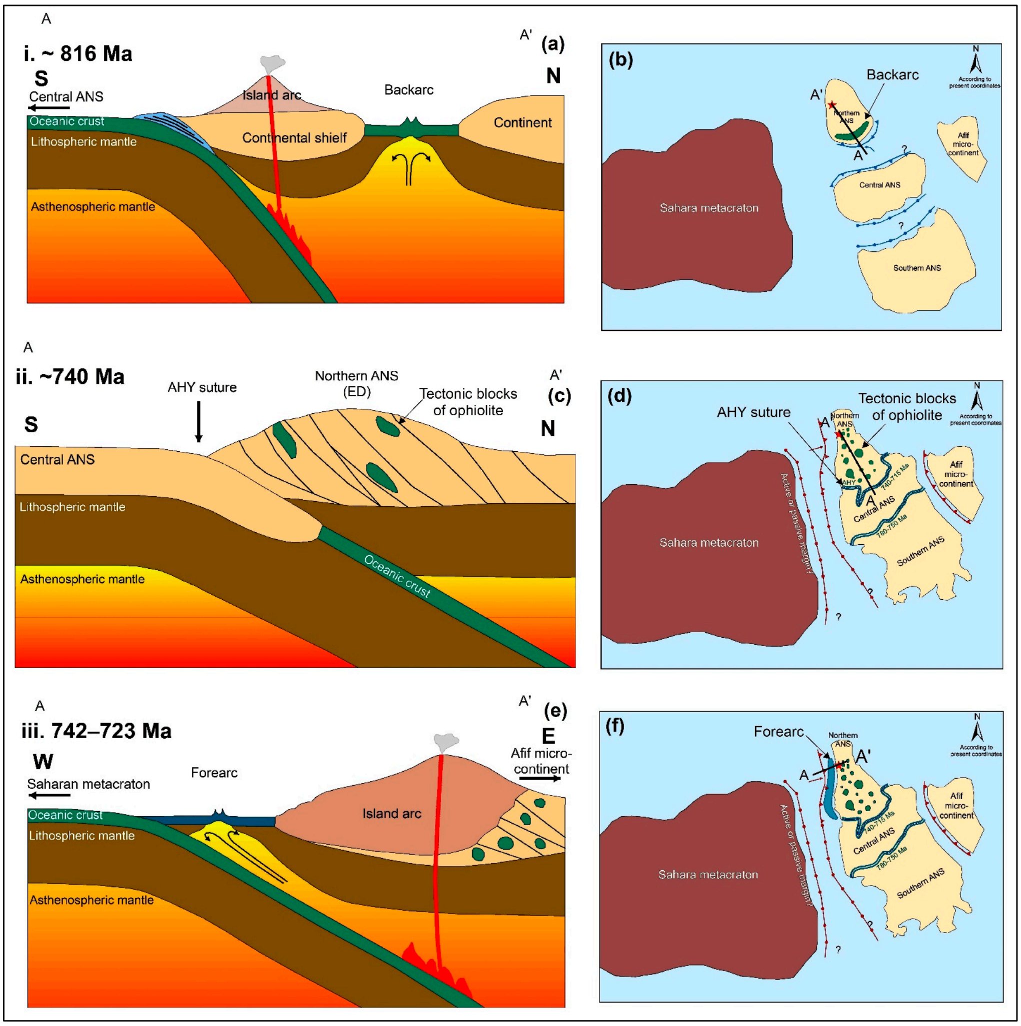

Figure 16. Tectonic evolutional model for the ED within north ANS: (**a**,**b**) the first stage N-dipping subduction occurred along the southern margin of the ED at ~816 Ma or earlier. During this subduction stage, a continental island arc formed with a bark-arc basin due to rifting in the margin of a thin old continental arc, producing arc-related plutonic and volcanic activities, which formed the tectonic blocks in the ophiolitic mélange; (**c**,**d**) collision occurred along the AHY suture at the south of ED; (**e**,**f**) the second stage of E-dipping subduction occurred along the western margin of the ED, resulting in the formation of an ophiolite sequence in a forearc basin during 742–723 Ma.

6.2. Petrogenesis and Tectonic Evolution of the Ophiolite Sequence and Felsic Dike Rocks (742–723 Ma)

The ophiolite sequence consists of serpentinized ultramafic rocks, ophiolitic gabbro, and basaltic rocks. The gabbro in the ophiolite sequence and felsic dike rocks show intrusion ages of 742 Ma and 723 Ma, respectively. The gabbro and basaltic rocks from the ophiolite sequence plotted in island arc tholeiite (IAT) and island arc basalt (IAB) fields in the Ti vs. V, Y vs. Cr, and Ti/40-Si/100-Sr tectonic discrimination diagrams (Figure 10a–c). Felsic dike rocks have an I-type affinity in the 10000Ga/Al vs. Na_2O + K_2O and SiO_2 vs. Zr diagrams and are plotted in volcanic arc tectonic setting in the Y vs. Nb diagram (Figure 10d–f). Similar interpretations were also provided from the gabbro with U–Pb zircon age of 736 Ma [10,21].

Most basaltic and felsic dike rocks give REE concentration between OIB and E-MORB with Nb–Ta negative troughs, and gabbro shows depleted LREEs, such as N-MORB, supporting their arc origin with backarc or forearc basins (Figure 11c,d). As the maturity of the backarc or forearc basin increased (concurrent with an increase in the width of the basin), the spreading center, initially located close to the arc during the initial stage, moved increasingly further away from the volcanic arc, resulting in a compositional change from N-MORB and E-MORB to OIB [68–71].

The trace element compositions of zircons from gabbro are plotted on the arc fields in the Th/U vs. Nb/Hf and Th/Nb vs. Hf/Th diagrams and the continental fields in the Y vs. U/Yb and Hf vs. U/Yb diagrams (Figure 8). The compositions of the zircons from felsic dike rocks are plotted on the arc field in the Th/U vs. Nb/Hf and Th/Nb vs. Hf/Th diagrams and on the overlapped fields between continental and oceanic zircons in the Y vs. U/Yb and Hf vs. U/Yb diagrams (Figure 8). These results suggest that the ophiolite sequence formed in an island arc tectonic setting along the margin of immature continental crust.

The serpentinized ultramafic rocks contain exceptionally low contents of Al_2O_3 (0.27–0.52 wt%) and CaO (0.18–0.23 wt%), and the Cr-spinels have a high Cr# and relatively low Mg#, which are characteristic of forearc peridotite. The spinels in them have a Cr# of 0.67–0.85 and TiO_2 content of 0.005–0.086 wt%, indicating their depleted nature. The compositions of the spinel and olivine also indicate that the serpentinized ultramafic rocks were a forearc mantle formed in the suprasubduction zone tectonic setting and that they experienced ~30%–40% of partial melting (Figure 14). The forearc character of serpentinized ultramafic rocks from the Fawakhir area was also reported by many authors [72,73].

These geochemical features indicate that the ophiolite sequence originated in ~742 Ma in a forearc basin associated with a suprasubduction zone, in which ophiolites show the geochemical features of island arcs and oceanic crust signature and are mostly formed by rifting directly above subducted oceanic lithosphere [74]. The ultramafic rocks may have undergone serpentinization during their uplift. The felsic dike rocks indicate that the subduction-related arc activities continued until 723 Ma (Figure 16c,d).

6.3. Tectonic Evolution of the Fawakhir Area with Clarifying Subduction Directions

The tectonic blocks in the ophiolitic mélange in the Fawakhir area were interpreted as being formed in the backarc basin associated with the continental island arc during ~816 Ma, implying the existence of a subduction zone along the AHY suture zone (Figure 2). It has, however, remained unclear whether the subduction (before the collision) along the AHY suture occurred toward the north [75–77] or the southeast [14,78]. During the subduction stage, the ophiolite rocks formed in the backarc basin along the southern margin of the ED. They were later tectonically emplaced as tectonic blocks from the southern ED to the central ED during the collision along the AHY suture [17,18]. This interpretation is supported by the distribution of ophiolitic mélange in the SED and CED, which supports the N-dipping subduction zone along the AHY suture in the southern margin of the ED. The N-dipping subduction was also interpreted from structural studies for ophiolite rocks at the AHY suture [76,77]. The depositional age of the ophiolitic mélange metasediments is ~750 Ma [22], indicating that they were deposited during the N-dipping subduction and that they incorporated tectonic blocks of the earlier ophiolite sequence during its deposition. Further studies concerning the ophiolitic mélange and tectonic blocks, including more age dating, will be needed to confirm the interpretation suggested in this study.

At the age of ~740–715 Ma, a collision along the AHY suture occurred [2,3,13]. However, in this study, ~742–723 Ma arc-related ophiolite rocks were found, indicating a new subduction event. Along the western margin of ED, the younger collision zone formed along the N-S Keraf suture zone between the ANS and Saharan metacraton. The N-S collision along the Keraf suture initiated ~640 Ma, suggesting that the second subduction existed before ~640 Ma [15,79]. The E-dipping direction of subduction along the N-S Keraf suture zone was interpreted based on the 740–700 Ma backarc signature volcanic rocks in the SED [6]. Further support for this interpretation comes from the N-S distribution of post-collisional igneous rocks along the ED, which have ages of ~635–580 Ma [80–82] because the post-collisional igneous rocks formed in the continental slab under which the slab break-off occurred between the subducted continental and oceanic slabs [83,84]. After the ophiolitic mélange thrusted on the ophiolite sequence during the collision, both of them were intruded during the post-collision stage by 630–600 Ma granite and granodiorite [19].

Two separate subductions are supported by the difference between the age of the tectonic blocks in the ophiolitic mélange (816 Ma) and that of the ophiolite sequence (742–723 Ma). Also, the different tectonic origins for them (backarc origin tectonic blocks in the ophiolitic mélange, and forearc origin ophiolite sequence) and different geochemical characters (depleted character for tectonic blocks in the ophiolitic mélange, and enriched character for the ophiolite sequence) indicate two separated subduction events.

7. Conclusions

The tectonic evolution of the Fawakhir area and the ED of Egypt was suggested based on an analysis of whole-rock geochemical composition, mineral chemistry, the trace element composition of zircon, and zircon U–Pb age dating as follows:

1. The gabbro from the ophiolitic mélange (GM-11), east of the Fawakhir area, gives an intrusion age of ~816 Ma, while the gabbro (GOS-48) and felsic dike rock (FD-28b) from the ophiolite sequence give an intrusion age of 742 Ma and 723 Ma, respectively;
2. The tectonic blocks from the ophiolitic mélange (816 Ma) formed in a back-arc basin in the continental island arc;
3. The rocks in the ophiolite sequence and intruded felsic dikes from the Fawakhir area (742–723 Ma) formed in a forearc basin in the continental-island arc;
4. At ~816 Ma or earlier, N-dipping subduction began along the southern margin of the ED. During this subduction stage, the margin of a thin old continental crust was changed into a continental island arc with rifting of the backarc basin, producing the island arc-related igneous plutonic and volcanic rocks;
5. During ~742–723 Ma, new island arc ophiolite sequences were formed at the Fawakhir area due to the second E-dipping subduction event along the western margin of the ED. During this later subduction stage, the new island arc-related igneous plutonic and volcanic rocks were produced with the opening of a forearc basin.

Supplementary Materials: The following supporting information can be downloaded at: https://www.mdpi.com/article/10.3390/min13081022/s1, Figure S1: Hand specimen photographs for rocks in the ophiolitic mélange. (a) gabbro (GM-11). (b) Gabbroic diorite (GDM-46). (c) Diabase (DM-50E). (d) Basaltic rocks (BM-40A). (e) Intermediate-volcanic rocks (AM-59). Figure S2: Hand specimen photographs for rocks in the ophiolite sequence: (a) Serpentinized ultramafic rock (SOS-2i). (b) Gabbro (GOS-48). (c) Basaltic rocks (BOS-25). (d) Felsic dike rocks (FD-28b). Table S1: LA–ICP–MS zircon U–Pb isotope and age dating results of the rocks from ophiolitic mélange, ophiolite sequence, and felsic dikes. Table S2: LA–ICP–MS zircon trace element and REE data (ppm) of the LA–ICP–MS zircon U–Pb isotopes and dating results of the rocks from ophiolitic mélange, ophiolite sequence, and felsic dike. Table S3: Whole-rock major and trace element data of the studied rocks from ophiolitic melange, ophiolite sequence and felsic dikes. Table S4: Representative composition of spinel, olivine, and orthopyroxene (Opx) from serpentinized ultramafic rock (SOS-3e) from ophiolite sequence, with description d standards used.

Author Contributions: Conceptualization, rock samples collection, data acquisition, data visualization, writing—original draft, review and editing, S.Y.; supervision, conceptualization, review, C.W.O.; data visualization, review, K.K.; rock samples collection, review, M.A. All authors have read and agreed to the published version of the manuscript.

Funding: This study was supported by the National Research Foundation of Korea (NRF-2017K1A1A2013180). Samar Yousef received support from the Global Korea Scholarship (GKS) Program of the National Institute for International Education (NIIED), a branch of the Republic of Korea's Ministry of Education.

Data Availability Statement: Not Applicable.

Acknowledgments: The authors would like to thank Hongfang Chen, the manager of the LA-ICP-MS instrument at Wuhan Sample Solution Analytical Technology Co., Ltd., China, as well as Choi Jinhyeok from the Petrology Lab at Jeonbuk National University and Ryu Jaeheung from Pertology Lab at Chonnam National University for their assistance during the EPMA analysis.

Conflicts of Interest: The authors declare that they have no known competing financial interests or personal relationships that could have appeared to influence the work reported in this paper.

References

1. Reymer, A.; Schubert, G. Phanerozoic addition rates to the continental crust and crustal growth. *Tectonics* **1984**, *3*, 63–77. [CrossRef]
2. Johnson, P.; Andresen, A.; Collins, A.; Fowler, A.; Fritz, H.; Ghebreab, W.; Kusky, T.; Stern, R. Late Cryogenian–Ediacaran history of the Arabian–Nubian Shield: A review of depositional, plutonic, structural, and tectonic events in the closing stages of the northern East African Orogen. *J. Afr. Earth Sci.* **2011**, *61*, 167–232. [CrossRef]
3. Collins, A.S.; Blades, M.L.; Merdith, A.S.; Foden, J.D. Closure of the Proterozoic Mozambique Ocean was instigated by a late Tonian plate reorganization event. *Commun. Earth Environ.* **2021**, *2*, 75. [CrossRef]
4. Loizenbauer, J.; Wallbrecher, E.; Fritz, H.; Neumayr, P.; Khudeir, A.; Kloetzli, U. Structural geology, single zircon ages and fluid inclusion studies of the Meatiq metamorphic core complex: Implications for Neoproterozoic tectonics in the Eastern Desert of Egypt. *Precambrian Res.* **2001**, *110*, 357–383. [CrossRef]
5. Gamal El Dien, H.; Li, Z.-X.; Abu Anbar, M.; Doucet, L.S.; Murphy, J.B.; Evans, N.J.; Xia, X.-P.; Li, J. The largest plagiogranite on Earth formed by re-melting of juvenile proto-continental crust. *Commun. Earth Environ.* **2021**, *2*, 138. [CrossRef]
6. Gamal El Dien, H.; Li, Z.-X.; Anbar, M.A.; Doucet, L.S.; Murphy, J.B.; Evans, N.J.; Xia, X.-P.; Li, J. Two-stage crustal growth in the Arabian-Nubian shield: Initial arc accretion followed by plume-induced crustal reworking. *Precambrian Res.* **2021**, *359*, 106211. [CrossRef]
7. Abd El-Naby, H.; Frisch, W. Geochemical constraints from the Hafafit Metamorphic Complex (HMC): Evidence of Neoproterozoic back-arc basin development in the central Eastern Desert of Egypt. *J. Afr. Earth Sci.* **2006**, *45*, 173–186. [CrossRef]
8. El-Shazly, A.; Khalil, K. Metamorphic and geochronologic constraints on the tectonic evolution of the Central Eastern Desert of Egypt. *Precambrian Res.* **2016**, *283*, 144–168. [CrossRef]
9. Abd El-Rahman, Y.; Polat, A.; Dilek, Y.; Fryer, B.; El-Sharkawy, M.; Sakran, S. Geochemistry and tectonic evolution of the neoproterozoic Wadi Ghadir ophiolite, eastern desert, Egypt. *Lithos* **2009**, *113*, 158–178. [CrossRef]
10. Abd El-Rahman, Y.; Polat, A.; Dilek, Y.; Fryer, B.J.; El-Sharkawy, M.; Sakran, S. Geochemistry and tectonic evolution of the Neoproterozoic incipient arc–forearc crust in the Fawakhir area, Central Eastern Desert of Egypt. *Precambrian Res.* **2009**, *175*, 116–134. [CrossRef]
11. Gray, D.R.; Foster, D.; Meert, J.; Goscombe, B.; Armstrong, R.; Trouw, R.; Passchier, C. A Damara orogen perspective on the assembly of southwestern Gondwana. *Geol. Soc. Lond. Spec. Publ.* **2008**, *294*, 257–278. [CrossRef]
12. CONOCO. *Geological Map of Egypt, Scale 1:500,000*; Egyptian General Petroleum Corporation-Conoco Coral: Cairo, Egypt, 1987.
13. Fritz, H.; Abdelsalam, M.; Ali, K.; Bingen, B.; Collins, A.; Fowler, A.; Ghebreab, W.; Hauzenberger, C.; Johnson, P.; Kusky, T. Orogen styles in the East African Orogen: A review of the Neoproterozoic to Cambrian tectonic evolution. *J. Afr. Earth Sci.* **2013**, *86*, 65–106. [PubMed]
14. Robinson, F.; Foden, J.; Collins, A.; Payne, J. Arabian Shield magmatic cycles and their relationship with Gondwana assembly: Insights from zircon U–Pb and Hf isotopes. *Earth Planet. Sci. Lett.* **2014**, *408*, 207–225. [CrossRef]
15. Abdelsalam, M.G.; Stern, R.J.; Copeland, P.; Elfaki, E.M.; Elhur, B.; Ibrahim, F.M. The Neoproterozoic Keraf Suture in NE Sudan: Sinistral transpression along the eastern margin of West Gondwana. *J. Geol.* **1998**, *106*, 133–148. [CrossRef]
16. El Ramly, M.F. A new geological map for the basement rocks in the Eastern and south Western Desert of Egypt, scale 1: 1,000,000. *Ann. Geol. Surv. Egypt* **1972**, *2*, 1–18.
17. Said, R. The geology of Egypt: Balkema. *Rotterdam Brookfield* **1990**, *734*, 676–677. [CrossRef]

18. Azer, M.K.; Stern, R.J. Neoproterozoic (835–720 Ma) serpentinites in the Eastern Desert, Egypt: Fragments of forearc mantle. *J. Geol.* **2007**, *115*, 457–472. [CrossRef]
19. Hamimi, Z.; El-Barkooky, A.; Frías, J.M.; Fritz, H.; Abd El-Rahman, Y. *The Geology of Egypt*; Springer: Berlin/Heidelberg, Germany, 2020.
20. Andresen, A.; El-Rus, M.A.A.; Myhre, P.I.; Boghdady, G.Y.; Corfu, F. U–Pb TIMS age constraints on the evolution of the Neoproterozoic Meatiq Gneiss dome, Eastern Desert, Egypt. *Int. J. Earth Sci.* **2009**, *98*, 481–497. [CrossRef]
21. Zoheir, B.; Abd El-Rahman, Y.; Kusky, T.; Xiong, F. New SIMS zircon U-Pb ages and oxygen isotope data for ophiolite nappes in the Eastern Desert of Egypt: Implications for Gondwana assembly. *Gondwana Res.* **2022**, *105*, 450–467. [CrossRef]
22. Ali, K.; Azer, M.; Gahlan, H.; Wilde, S.; Samuel, M.; Stern, R. Age constraints on the formation and emplacement of Neoproterozoic ophiolites along the Allaqi–Heiani Suture, South Eastern Desert of Egypt. *Gondwana Res.* **2010**, *18*, 583–595. [CrossRef]
23. Wilde, S.; Youssef, K. Significance of SHRIMP U-Pb dating of the imperial porphyry and associated Dokhan volcanics, Gebel Dokhan, north Eastern Desert, Egypt. *J. Afr. Earth Sci.* **2000**, *31*, 403–413. [CrossRef]
24. Breitkreuz, C.; Eliwa, H.; Khalaf, I.; El Gameel, K.; Bühler, B.; Sergeev, S.; Larionov, A.; Murata, M. Neoproterozoic SHRIMP U–Pb zircon ages of silica-rich Dokhan volcanics in the North Eastern Desert, Egypt. *Precambrian Res.* **2010**, *182*, 163–174. [CrossRef]
25. Moghazi, A.-K.M.; Ali, K.A.; Wilde, S.A.; Zhou, Q.; Andersen, T.; Andresen, A.; El-Enen, M.M.A.; Stern, R.J. Geochemistry, geochronology, and Sr–Nd isotopes of the Late Neoproterozoic Wadi Kid volcano-sedimentary rocks, Southern Sinai, Egypt: Implications for tectonic setting and crustal evolution. *Lithos* **2012**, *154*, 147–165. [CrossRef]
26. Wilde, S.; Youssef, K. A re-evaluation of the origin and setting of the Late Precambrian Hammamat Group based on SHRIMP U–Pb dating of detrital zircons from Gebel Umm Tawat, North Eastern Desert, Egypt. *J. Geol. Soc.* **2002**, *159*, 595–604. [CrossRef]
27. Bezenjani, R.N.; Pease, V.; Whitehouse, M.J.; Shalaby, M.; Kadi, K.; Kozdroj, W. Detrital zircon geochronology and provenance of the Neoproterozoic Hammamat Group (Igla Basin), Egypt and the Thalbah Group, NW Saudi Arabia: Implications for regional collision tectonics. *Precambrian Res.* **2014**, *245*, 225–243. [CrossRef]
28. Abdel-Karim, A.A.M.; Azer, M.K.; El-Shafei, S.A. Petrology and Geochemistry of Some Ophiolitic Metaperidotites from the Eastern Desert of Egypt: Insights into Geodynamic Evolution and Metasomatic Processes. *Acta Geol. Sin.-Engl. Ed.* **2021**, *95*, 1139–1157. [CrossRef]
29. Lee, B.C.; Oh, C.W.; Yi, K. Geochemistry, zircon U–Pb ages, and Hf isotopic compositions of Precambrian gneisses in the Wonju–Jechon area of the southern Gyeonggi Massif: Implications for the Precambrian tectonic evolution of Korea and northeast Asia. *Precambrian Res.* **2016**, *283*, 169–189. [CrossRef]
30. Wiedenbeck, M.; Alle, P.; Corfu, F.; Griffin, W.L.; Meier, M.; Oberli, F.v.; Quadt, A.v.; Roddick, J.; Spiegel, W. Three natural zircon standards for U-Th-Pb, Lu-Hf, trace element and REE analyses. *Geostand. Newsl.* **1995**, *19*, 1–23. [CrossRef]
31. Stephen, A.W.; Robert, L.W. *Certificate of Analysis Standard Reference Material 610*; National Institute of Standard & Technology: Gaithersburg, MD, USA, 2012.
32. Sláma, J.; Košler, J.; Condon, D.J.; Crowley, J.L.; Gerdes, A.; Hanchar, J.M.; Horstwood, M.S.; Morris, G.A.; Nasdala, L.; Norberg, N. Plešovice zircon—A new natural reference material for U–Pb and Hf isotopic microanalysis. *Chem. Geol.* **2008**, *249*, 1–35. [CrossRef]
33. Liu, Y.; Gao, S.; Hu, Z.; Gao, C.; Zong, K.; Wang, D. Continental and oceanic crust recycling-induced melt–peridotite interactions in the Trans-North China Orogen: U–Pb dating, Hf isotopes and trace elements in zircons from mantle xenoliths. *J. Petrol.* **2010**, *51*, 537–571. [CrossRef]
34. Liu, Y.; Hu, Z.; Gao, S.; Günther, D.; Xu, J.; Gao, C.; Chen, H. In situ analysis of major and trace elements of anhydrous minerals by LA-ICP-MS without applying an internal standard. *Chem. Geol.* **2008**, *257*, 34–43. [CrossRef]
35. Kawaguchi, K.; Oh, C.W.; Jeong, J.W. Geochemistry, zircon UPb ages and LuHf isotopes of Triassic plutons in the eastern Gyeonggi Massif, Korean Peninsula: Magma genesis and geodynamic implications for East Asia. *Lithos* **2023**, *436*, 106955. [CrossRef]
36. Ludwig, K. User's Manual for Isoplot 3.6 A Geochronological Toolkit for Microsoft Excel, Berkeley Geochron. *Cent. Spec. Publ* **2008**, *4*, 77.
37. Yang, J.; Cawood, P.A.; Du, Y.; Huang, H.; Huang, H.; Tao, P. Large Igneous Province and magmatic arc sourced Permian–Triassic volcanogenic sediments in China. *Sediment. Geol.* **2012**, *261*, 120–131. [CrossRef]
38. Grimes, C.B.; John, B.E.; Kelemen, P.; Mazdab, F.; Wooden, J.; Cheadle, M.J.; Hanghøj, K.; Schwartz, J. Trace element chemistry of zircons from oceanic crust: A method for distinguishing detrital zircon provenance. *Geology* **2007**, *35*, 643–646. [CrossRef]
39. Wang, M.; Guo, W.; Yang, W. Detrital zircon trace elements from the Mesozoic Jiyuan Basin, central China and its implication on tectonic transition of the Qinling Orogenic Belt. *Open Geosci.* **2019**, *11*, 125–139. [CrossRef]
40. Middlemost, E.A. Naming materials in the magma/igneous rock system. *Earth-Sci. Rev.* **1994**, *37*, 215–224. [CrossRef]
41. Irvine, T.N.; Baragar, W. A guide to the chemical classification of the common volcanic rocks. *Can. J. Earth Sci.* **1971**, *8*, 523–548. [CrossRef]
42. Shervais, J.W. Ti-V plots and the petrogenesis of modern and ophiolitic lavas. *Earth Planet. Sci. Lett.* **1982**, *59*, 101–118. [CrossRef]
43. Pearce, J.A. Trace element characteristics of lavas from destructive plate boundaries. In *Orogenic Andesites and Related Rocks*; John Wiley and Son: Chichester, UK, 1982; pp. 528–548.
44. Dilek, Y.; Furnes, H.; Shallo, M. Suprasubduction zone ophiolite formation along the periphery of Mesozoic Gondwana. *Gondwana Res.* **2007**, *11*, 453–475. [CrossRef]
45. Vermeesch, P. Tectonic discrimination diagrams revisited. *Geochem. Geophys. Geosystems* **2006**, *7*, 55.

46. Whalen, J.B.; Currie, K.L.; Chappell, B.W. A-type granites: Geochemical characteristics, discrimin,ation and petrogenesis. *Contrib. Mineral. Petrol.* **1987**, *95*, 407–419. [CrossRef]
47. Collins, W.; Beams, S.; White, A.; Chappell, B. Nature and origin of A-type granites with particular reference to southeastern Australia. *Contrib. Mineral. Petrol.* **1982**, *80*, 189–200. [CrossRef]
48. Pearce, J.A.; Harris, N.B.; Tindle, A.G. Trace element discrimination diagrams for the tectonic interpretation of granitic rocks. *J. Petrol.* **1984**, *25*, 956–983. [CrossRef]
49. Sun, S.-S.; McDonough, W.F. Chemical and isotopic systematics of oceanic basalts: Implications for mantle composition and processes. *Geol. Soc. Lond. Spec. Publ.* **1989**, *42*, 313–345. [CrossRef]
50. Ishii, T. Petrological studies of peridotites from diapiric serpentinite seamounts in the Izu-Ogasawara-Mariana forearc, Leg 125. *Proc. Ocean Drill. Program Sci. Results Coll. Stn. TX USA* **1992**, *125*, 445–485.
51. Dick, H.J.; Bullen, T. Chromian spinel as a petrogenetic indicator in abyssal and alpine-type peridotites and spatially associated lavas. *Contrib. Mineral. Petrol.* **1984**, *86*, 54–76. [CrossRef]
52. Kamenetsky, V.S.; Crawford, A.J.; Meffre, S. Factors controlling chemistry of magmatic spinel: An empirical study of associated olivine, Cr-spinel and melt inclusions from primitive rocks. *J. Petrol.* **2001**, *42*, 655–671. [CrossRef]
53. Xu, Y.; Chen, S.; Parlak, O.; Arai, S.; Dönmez, C.; Hong, J. Discovery of extremely high-Al podiform chromitites from the Lycian (Marmaris) ophiolite, SW Turkey: Implications for chromitite genesis. *Ore Geol. Rev.* **2020**, *127*, 103817. [CrossRef]
54. Khedr, M.Z.; Arai, S. Peridotite-chromitite complexes in the Eastern Desert of Egypt: Insight into Neoproterozoic sub-arc mantle processes. *Gondwana Res.* **2017**, *52*, 59–79. [CrossRef]
55. Stern, R.J.; Johnson, P.R.; Kröner, A.; Yibas, B. Neoproterozoic ophiolites of the Arabian-Nubian shield. *Dev. Precambrian Geol.* **2004**, *13*, 95–128.
56. Morimoto, N. Nomenclature of pyroxenes. *Mineral. J.* **1989**, *14*, 198–221. [CrossRef]
57. Deer, W.A.; Howie, R.A.; Zussman, J. *An Introduction to the Rock-Forming Minerals*; Mineralogical Society of Great Britain and Ireland: London, UK, 2013.
58. Lindsley, D.H. *Oxide Minerals: Petrologic and Magnetic Significance*; Walter de Gruyter GmbH & Co KG: Berlin, Germany, 2018; Volume 25.
59. Cameron, W.; McCulloch, M.; Walker, D. Boninite petrogenesis: Chemical and Nd-Sr isotopic constraints. *Earth Planet. Sci. Lett.* **1983**, *65*, 75–89. [CrossRef]
60. Stern, R.J.; Bloomer, S.H. Subduction zone infancy: Examples from the Eocene Izu-Bonin-Mariana and Jurassic California arcs. *Geol. Soc. Am. Bull.* **1992**, *104*, 1621–1636. [CrossRef]
61. Elias, S.; Alderton, D. *Encyclopedia of Geology*; Academic Press: Cambridge, MA, USA, 2020.
62. Shervais, J.W.; Reagan, M.K.; Godard, M.; Prytulak, J.; Ryan, J.G.; Pearce, J.A.; Almeev, R.R.; Li, H.; Haugen, E.; Chapman, T. Magmatic response to subduction initiation, Part II: Boninites and related rocks of the Izu-Bonin Arc from IODP Expedition 352. *Geochem. Geophys. Geosystems* **2021**, *22*, e2020GC009093. [CrossRef]
63. Falloon, T.J.; Crawford, A.J. The petrogenesis of high-calcium boninite lavas dredged from the northern Tonga ridge. *Earth Planet. Sci. Lett.* **1991**, *102*, 375–394. [CrossRef]
64. Smithies, R. Archaean boninite-like rocks in an intracratonic setting. *Earth Planet. Sci. Lett.* **2002**, *197*, 19–34. [CrossRef]
65. Shang, C.K.; Morteani, G.; Satir, M.; Taubald, H. Neoproterozoic continental growth prior to Gondwana assembly: Constraints from zircon–titanite geochronology, geochemistry and petrography of ring complex granitoids, Sudan. *Lithos* **2010**, *11*, 61–81. [CrossRef]
66. Stern, R.J. The anatomy and ontogeny of modern intra-oceanic arc systems. *Geol. Soc. Lond. Spec. Publ.* **2010**, *338*, 7–34. [CrossRef]
67. Winter, J.D. *Principles of Igneous and Metamorphic Petrology*; Pearson Education: London UK, 2013.
68. Saunders, A.D.; Tarney, J. Geochemical characteristics of basaltic volcanism within back-arc basins. *Geol. Soc. Lond. Spec. Publ.* **1984**, *16*, 59–76. [CrossRef]
69. Taylor, B.; Martinez, F. Back-arc basin basalt systematics. *Earth Planet. Sci. Lett.* **2003**, *210*, 481–497. [CrossRef]
70. Pearce, J.A.; Stern, R.J. Origin of back-arc basin magmas: Trace element and isotope perspectives. *Back-Arc Spreading Syst. Geol. Biol. Chem. Phys. Interact.* **2006**, *166*, 63–86.
71. Suda, Y.; Hayasaka, Y.; Kimura, K. Crustal evolution of a Paleozoic intra-oceanic island-arc-back-arc basin system constrained by the geochemistry and geochronology of the Yakuno Ophiolite, Southwest Japan. *J. Geol. Res.* **2014**, *2014*, 652484. [CrossRef]
72. Abdel-Karim, A.-A.M.; Ali, S.; El-Shafei, S.A. Mineral chemistry and geochemistry of ophiolitic metaultramafics from Um Halham and Fawakhir, Central Eastern Desert, Egypt. *Int. J. Earth Sci.* **2018**, *107*, 2337–2355. [CrossRef]
73. Hamdy, M.M.; Harraz, H.Z.; Aly, G.A. Pan-African (intraplate and subduction-related?) metasomatism in the Fawakhir ophiolitic serpentinites, Central Eastern Desert of Egypt: Mineralogical and geochemical evidences. *Arab. J. Geosci.* **2013**, *6*, 13–33. [CrossRef]
74. Pearce, J.A.; Lippard, S.; Roberts, S. Characteristics and tectonic significance of supra-subduction zone ophiolites. *Geol. Soc. Lond. Spec. Publ.* **1984**, *16*, 77–94. [CrossRef]
75. Abdelsalam, M.G.; Stern, R.J. Structure of the late Proterozoic Nakasib suture, Sudan. *J. Geol. Soc.* **1993**, *150*, 1065–1074. [CrossRef]
76. Kusky, T.M.; Ramadan, T.M. Structural controls on Neoproterozoic mineralization in the South Eastern Desert, Egypt: An integrated field, Landsat TM, and SIR-C/X SAR approach. *J. Afr. Earth Sci.* **2002**, *35*, 107–121. [CrossRef]
77. Abdeen, M.M.; Abdelghaffar, A.A. Syn-and post-accretionary structures in the Neoproterozoic Central Allaqi-Heiani suture zone, Southeastern Egypt. *Precambrian Res.* **2011**, *185*, 95–108. [CrossRef]

78. Fitches, W.; Graham, R.; Hussein, I.; Ries, A.; Shackleton, R.; Price, R. The late Proterozoic ophiolite of Sol Hamed, NE Sudan. *Precambrian Res.* **1983**, *19*, 385–411. [CrossRef]
79. Bailo, T.; Schandelmeier, H.; Franz, G.; Sun, C.-H.; Stern, R. Plutonic and metamorphic rocks from the Keraf Suture (NE Sudan): A glimpse of Neoproterozoic tectonic evolution on the NE margin of W. Gondwana. *Precambrian Res.* **2003**, *123*, 67–80. [CrossRef]
80. Ali, K.; Andresen, A.; Stern, R.; Manton, W.; Omar, S.; Maurice, A. U-Pb zircon and Sr-Nd-Hf isotopic evidence for a juvenile origin of the c 634 Ma El-Shalul granite, Central Eastern Desert, Egypt. *Geol. Mag.* **2012**, *149*, 783–797. [CrossRef]
81. Ali, K.A.; Moghazi, A.-K.M.; Maurice, A.E.; Omar, S.A.; Wang, Q.; Wilde, S.A.; Moussa, E.M.; Manton, W.I.; Stern, R.J. Composition, age, and origin of the ~620 Ma Humr Akarim and Humrat Mukbid A-type granites: No evidence for pre-Neoproterozoic basement in the Eastern Desert, Egypt. *Int. J. Earth Sci.* **2012**, *101*, 1705–1722. [CrossRef]
82. Skublov, S.G.; Gawad, A.E.A.; Levashova, E.V.; Ghoneim, M.M. U–Pb geochronology, REE and trace element geochemistry of zircon from El Fereyid monzogranite, south Eastern Desert, Egypt. *J. Mineral. Petrol. Sci.* **2021**, *116*, 220–233. [CrossRef]
83. Lee, B.C.; Park, J.H.; Oh, C.W.; Yi, K. Metamorphic and magmatic evolution of the Paleoproterozoic gneisses in the Sancheong area, Yeongnam Massif, South Korea, and their implications to the tectonics in the Northeast Asia. *Precambrian Res.* **2017**, *298*, 439–461. [CrossRef]
84. Yi, S.-B.; Oh, C.W.; Choi, S.-G.; Seo, J. A study on the Mesozoic Magmatism in the Dangjin Area, Western Gyeonggi Massif, Korea. *J. Petrol. Soc. Korea* **2019**, *28*, 85–109.